J. Fluid Mech. (2006), *vol.* 558, *pp.* 1–32.
doi:10.1017/S0022112006009207 Printed in the United Kingdom

Experimental study of a Neimark–Sacker bifurcation in axially forced Taylor–Couette flow

By MANISH SINHA[1], IOANNIS G. KEVREKIDIS[2] AND ALEXANDER J. SMITS[1]

[1]Department of Mechanical and Aerospace Engineering, Princeton University Princeton, NJ 08544-0710, USA

[2]Department of Chemical Engineering, PACM and Mathematics, Princeton University, Princeton, NJ 08544-0710, USA

(Received 4 March 2003 and in revised form 14 November 2005)

A variation of the classical Taylor–Couette system is studied where, with the outer cylinder stationary, the inner cylinder rotates at constant angular velocity while executing harmonic oscillations in the axial direction. Experiments reveal a Hopf (Neimark–Sacker) bifurcation from a limit cycle to a torus. Alternating bands of frequency-locked and quasi-periodic flow are observed and identified. Power spectral plots and (delay reconstructed) Poincaré maps are used to characterize the temporal dynamics. Results are presented on the rotation number variation across parameter space, the shape and growth of frequency-locked resonance horns, and the spatial development of the flow considerably beyond the primary transition surface.

1. Introduction

The review by Davis (1976) and numerical work by Marques, Lopez & Iranzo (2002) show that when flows are subject to external time-periodic forcing they are susceptible to complex spatio-temporal instabilities. Strong motivation for investigating such flows arises from their widespread technological importance (for instance, their occurrence in pumping processes) and the opportunity to explore rich dynamical behaviour in fluid systems. Systems exhibiting spatio-temporal instabilities are often complicated, and so relatively simple representative set-ups can be useful in attempts to isolate and understand the role played by the specific instability mechanisms that give rise to the observed flow states.

In general, it is difficult to predict quantitatively the response of a dissipative system to externally applied forcing. When a system is parametrically forced, complex temporal dynamical phenomena (such as frequency-locking, quasi-periodicity and chaos) often arise. Here, frequency locking or 'resonance' refers to a strong interplay and coupling between the external forcing frequency and one of the system's natural frequencies. Regions in parameter space (defined later by non-dimensional parameters) exist where such a relation between these two frequencies persists (that is, their ratio remains constant and equal to a rational number) for entire intervals of forcing frequencies and amplitudes.

Frequency locking and quasi-periodicity are typical of the dynamical behaviour observed when a periodic oscillation loses stability. If it loses stability through a Hopf bifurcation it may do so in three distinct generic ways, the precise manner depending on how the eigenvalues of the (monodromy) matrix associated with the instability

exit the unit circle in the complex plane (Guckenheimer & Holmes 1983). The first two types of crossing correspond to codimension-1 bifurcations; crossing through $+1$ implies a saddle-node bifurcation, while crossing through -1 implies a period doubling bifurcation. The third possibility (which is the case of interest here) involves a pair of complex conjugate eigenvalues ($\alpha \pm i\beta$) simultaneously crossing the unit circle, and corresponds to a Hopf bifurcation (which for limit cycles is also referred to as a Neimark–Sacker bifurcation). If this bifurcation occurs in the absence of any hysteresis (that is, if it is supercritical in character), the instability leads to a stable attractor close to the original limit cycle.

This new attractor is a two-dimensional invariant torus T^2. The resulting solutions of the instability lie on this torus, and may be quasi-periodic (winding themselves densely on the surface of the torus), or periodic, that is, frequency-locked (winding themselves periodically around the torus surface to form a closed spiral). A new frequency (associated with the angle at which the eigenvalue pair exits the unit circle) emerges via this bifurcation, and two parameters are now necessary to unravel all the possible dynamics, which include alternating regions of frequency-locking and quasi-periodic motion (see, for example, Bergé, Pomeau & Vidal (1984)).

Neimark–Sacker bifurcations have been found in several low-dimensional ODE systems, such as in chemical reactors (Kai & Tomita 1979; Keverekidis, Schmidt & Aris 1986) and chemostats (Pavlou & Kevrekidis 1992). Here, we are interested in a hydrodynamic system (Taylor–Couette flows with spatio-temporal forcing) governed by a set of dissipative PDEs. When such a system is periodically forced, we expect initially a periodic solution with the period of the forcing. If, at higher forcing amplitudes, this 'entrained' base periodic solution loses stability, a parametric resonance governed by a Neimark–Sacker bifurcation is expected. Neimark–Sacker bifurcations have been observed experimentally in unforced systems such as thermal convection (Chiffaudel & Fauve 1987; Ecke & Kevrekidis 1988; Glazier & Libchaber 1988) and vortex breakdown flow (Stevens, Lopez & Cantwell 1999).

The motivation for the present study lies in a series of related experimental and numerical investigations. The numerical work of Hu & Kelly (1995) demonstrated the possibility of achieving significant flow control (delay of the onset of instability) through periodic forcing in closed systems. Specifically, they computed a large degree of stabilization of the base flow in an infinitely long Taylor–Couette flow via axial oscillations of the inner cylinder. Parallel experimental work by Weisberg, Kevrekidis & Smits (1997) illustrated, for the first time, the stabilizing effect of axial oscillations of the inner cylinder on the critical rotation rate for the initial transition to Taylor vortex flow (TVF). The degree of stabilization observed in the experiments exceeded that of the numerical study, and Marques & Lopez (1997) showed that the principal reason for this discrepancy was due to the presence of endwalls and curvature effects in the experiment. Their results agreed remarkably well with those of Weisberg *et al.* (1997).

While the majority of the primary transitions documented by Weisberg *et al.* led to the formation of axisymmetric Taylor cells, Weisberg (1996) reported the appearance of non-axisymmetric cells as the primary transition for forced Taylor–Couette flow (specifically restricted to large amplitudes and small frequencies of forcing). The vortices, upon formation, were not normal to the cylinder axis (as in axisymmetric unforced Taylor–Couette flow) but tilted. These observations were initially viewed as the manifestation of a higher-order instability and were grouped together with other 'anomalous' observations. A Floquet analysis by Marques & Lopez (1997) considered the effect of axially and azimuthally periodic perturbations to the time-dependent base

flow. They too found that in narrow windows of parameter space, corresponding to large forcing amplitudes and small frequencies of the forcing, the primary bifurcation of the base state led to a non-axisymmetric flow. A key contribution of their work was the prediction of regions of complex spatio-temporal instabilities that give rise to the dynamics within this window. Marques & Lopez (2000) focused on these narrow windows in parameter space and discovered strong temporal resonances as well as competition between various spatial modes that were simultaneously excited. An excitation diagram illustrating the critical surface for the bifurcation, and the strong resonances to be expected, was presented. Floquet analysis is, of course, linearized around a base flow and as such applies only close to the bifurcation point; no information on the postcritical development after the bifurcation was obtained.

Beyond the criticality threshold into the nonlinear regime, the torus is often observed to break down and the flow becomes temporally chaotic. Such regions are the focus of the latter part of this paper. At criticality, inclined wavy Taylor spirals form. Their inclination (with respect to the cylinder axis) varies periodically with time. The Taylor spirals are physically characterized by two properties: an azimuthal wavenumber n and an axial wavenumber k. In any hydrodynamic system, as the parameters leading to a Neimark–Sacker bifurcation change, then so do the spatial properties of the bifurcating solution. That is, in our system, the axial wavenumber k and the azimuthal wavenumber n may change. Whereas the angle of inclination of the spirals varies periodically in time, the wavenumbers do not. They are fixed in time for a given mode (or flow state) and so, for practical convenience, we limit ourselves to n and k when attempting to characterize the wavy spiral states.

For low-dimensional systems, the dynamics resulting from a Neimark–Sacker bifurcation are characterized by a certain temporal complexity, involving a two-parameter interplay between quasi-periodicity and frequency-locking (resonance). For extended systems, such as the hydrodynamic system under investigation, the bifurcation can also lead to the excitation of modes with differing spatial structure. The spatial and temporal interactions between the various modes can lead to subsequent complicated spatio-temporal behaviour; in particular, we have explored the spatial structure and changes that occur during such a torus breakdown.

We have attempted to define the spatial characteristics of the flow through the (n, k) pair, though the uniqueness of the flow state cannot be guaranteed. Prior to transition, $n = 0$ and $k = 0$. Beyond criticality, the variation in (n, k) contains information pertaining to: (i) which wavenumber dominates; (ii) how the dominant wavenumber varies with axial and azimuthal Reynolds number; and (iii) whether there is any apparent connection between changes in the temporal behaviour of the bifurcated solution and its spatial properties. The expected variation in (n, k) is not clear, except that it will result from a nonlinear interaction between the circulation within the Taylor cells and the time-periodic axial flow between the cells. Wereley & Lueptow (1998) investigated the effect of constant annular Poiseuille flow on circular Couette flow (CCF) and found increasing axial wavenumber with axial Reynolds number. The interaction of CCF with time-periodic annular Poiseuille flow has not, to our knowledge, been previously investigated.

The principal contribution of the present work is the detailed description of the Neimark–Sacker instability in this flow beyond the immediate neighbourhood of the bifurcation surface. First, we investigate the physical manifestation of the bifurcated flow states and their subsequent spatial destabilization, the variation of the rotation number (the ratio of the bifurcation frequency to the forcing frequency) along 'cuts' in general parameter space, and the shape and growth of the frequency-locked

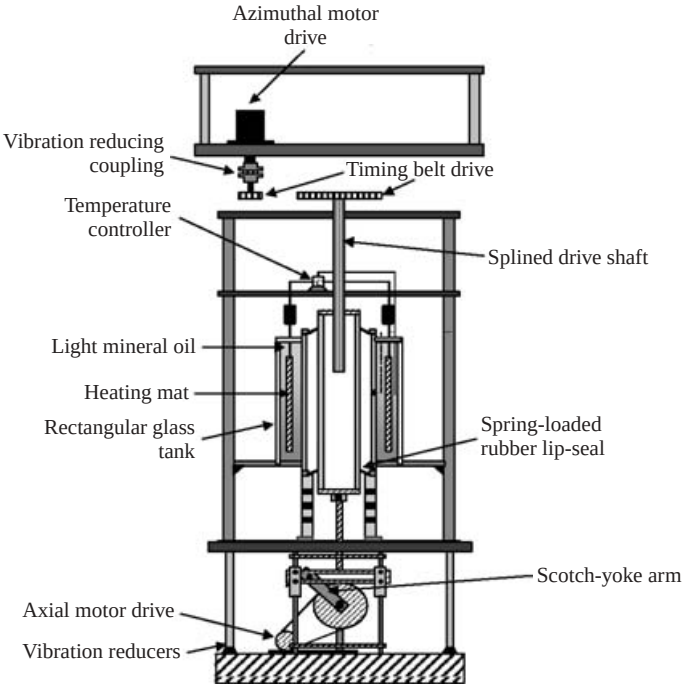

FIGURE 1. Diagram of the set-up, including modifications made to the original apparatus.

resonance horns (these are regions which contain the frequency-locked dynamics). Taken as a whole, these experiments represent the first attempt to explore the physical manifestation of the instability in regions that lie considerably beyond the instability threshold. Where possible, comparisons to related numerical work are made. In addition, we investigate the postcritical spatial behaviour of the bifurcated flow states, particularly the response of wavy vortex flow to increasing axial forcing, the response of a non-axisymmetric $n \neq 0$ mode located just above the critical surface to increasing rotation rates, and the possible correlation among changes in the postcritical spatial structure and temporal dynamics.

2. Experimental techniques

2.1. *Taylor–Couette apparatus*

The apparatus used in this study, shown in figure 1, was a modified version of that used by Weisberg *et al.* (1997). The stainless steel inner cylinder has an outer diameter of 3.003 ± 0.001 in (76.28 ± 0.03 mm) while the clear acrylic outer cylinder has an inner diameter of 3.318 ± 0.001 in (84.28 ± 0.03 mm) and thickness of 0.466 in (11.83 mm). (These tolerances were determined by the accuracy level of the professionally machined cylinders.) The upper and lower ends of the test section are bounded with watertight seals. A water-tight spring-loaded rubber lip seal is used at the lower end of the inner cylinder while an end cap machined from Delrin™ is used to seal the upper end of the test section. The gap width d is 4 mm, and the length of the test section $L = 152d$ so that endwall effects are minimized in comparison to many prior experiments (Cole 1976). Cole noted that endwalls affect the flow dynamics only in facilities with aspect ratio L/d less than about 40. This value is related to

studies without axial forcing, and no such study exists for the case when forcing is present. However, the observed transition Reynolds number for the onset of unforced Taylor vortex flow agrees to within experimental uncertainty with that predicted by Marques & Lopez (1997) for the case of infinitely long cylinders.

The inner cylinder is capable of two independent motions, azimuthal rotation and axial translation. Azimuthal rotation is imparted via a stepper motor driven in half-stepping mode which, combined with a 2:1 timing belt drive, performs 800 steps rev^{-1} of the inner cylinder. The axial motion is controlled by a separate stepper motor operating at 1000 steps rev^{-1} driving a Scotch-yoke mechanism. The effect of the stepping action on the flow dynamics can be safely assumed to be negligible because the investigations of Donnelly (1960), in which the effects of time modulation of the inner cylinder rotational speed were measured for various radius ratios, showed that no measurable effects should be observed for extraneous frequencies 800 times larger than the rotational frequency. The inner cylinder motion was characterized by typical angular and axial frequencies of about 0.1–0.2 Hz, angular and axial velocities of about $20\,\text{mm}\,\text{s}^{-1}$ and $100\,\text{mm}\,\text{s}^{-1}$, and a stroke length of about 100 mm.

It is important to quantify the effects of eccentricity in the alignment of the cylinders. The total maximum eccentricity measured by a spring-loaded dial indicator was 0.001 in 0.03 mm or 0.6 % of the gap width. According to Cole (1976), this changes the critical Reynolds number by less than 1%. Coupled with the excellent agreement found between our measurement of transition Reynolds number and the numerical prediction for the unforced case, it is reasonable to assume that eccentricity plays a negligible role in the dynamics of the flow.

The inner and outer cylinder radii are denoted by r_i and r_o, respectively. The incompressible fluid has kinematic viscosity ν. The inner cylinder rotates with angular velocity Ω while executing axial oscillations with frequency ω_f and experiences a maximum axial translational speed U. The axial and azimuthal Reynolds numbers are defined by:

$$Re_{ax} = Ud/\nu, \tag{2.1}$$

$$Re_{\Omega} = \Omega d r_i/\nu. \tag{2.2}$$

The forcing frequency is non-dimensionalized by the viscous time scale so that

$$\overline{\omega} = \omega_f d^2/\nu. \tag{2.3}$$

Finally, the two frequencies may be related via the applied frequency ratio

$$f_{app} = \omega_f/\Omega, \tag{2.4}$$

where a high f_{app} means that the inner cylinder executes many axial oscillations during one azimuthal rotation.

The working fluid is a 20:1 mixture of water and Kalliroscope AQ-1000 rheoscopic concentrate. The flakes align with the local shear stress and are effective for visualizing parallel shear flows, and the results from Savas (1985) suggest that such a technique should provide an accurate representation of the flow field in Taylor–Couette flow. The viscosity–temperature relationship of the working fluid was obtained from a calibration performed by the Energy Materials Testing Laboratory and can be found in Weisberg (1996).

Two major modifications were made to Weisberg's original apparatus. First, in order to reduce vibration levels produced by gears and driving mechanisms, a large framework was attached to the experiment at three points and also to a laboratory wall. The outer cylinder was attached to this frame via a rigid semi-circular collar.

The rotational stepping motor was connected to the 2:1 timing belt drive by a flexible loose-fitting coupling. This coupling substantially reduced the level of vibrations originating from the motor that were transmitted to the inner cylinder. Second, a glass tank containing light mineral oil was installed to enclose the outer cylinder. The oil in the glass tank substantially aided visualization of the flow by reducing stray light reflections originating from various surfaces, and it eliminated virtually all refraction effects when viewing the flow at an angle to the outer cylinder (the index of refraction of the clear acrylic is 1.49 while that of the mineral oil is 1.51). The oil also acted as a thermal insulator for the fluid in the test section since it has a high specific heat capacity.

The temperature must be controlled precisely because it has a strong effect on the fluid viscosity: a 0.1 °C change produces a change in viscosity ν, and hence Reynolds number, of about 2 %. A K-type thermocouple was placed flush with the inner surface of the outer cylinder roughly equidistant from the upper and lower ends of the annulus. The absolute accuracy of the thermocouples used is better than ± 1°C. Thermocouples were also used to monitor the temperature at various points in the oil bath, at the ends of the annulus and around the outer cylinder circumference. Azimuthal temperature variation on the outer cylinder did not exceed 0.1°C while the axial variation did not exceed 0.2°C. During data acquisition, the oil was heated slightly above ambient temperature with two fully submerged 254 mm $\times$ 127 mm 250 W heating mats and circulated continuously by two electric impeller mixers submerged in the oil and placed approximately at the centre of the tank. The oil was maintained to within ± 0.06°C of a fixed reference temperature (at a reference point in the tank) by an Omega CN76000 microprocessor-based feedback temperature controller. Because of the large thermal inertia of the oil, the working fluid took several hours to reach stable temperature. Even without the feedback control, the fluctuations in temperature were often within the ± 0.10 °C limit.

The experimental measurement errors in the Reynolds numbers and frequency estimates arise from errors in measuring $U, d, \nu, \Omega, r_i, d$ and ω_f. The maximum percentage errors (as opposed to the r.m.s. error) in determining the dimensionless parameters, calculated using the methods described by Bendat & Piersol (1966), are $\delta Re_{ax}/Re_{ax} = 2.0\%$, $\delta Re_{\Omega}/Re_{\Omega} = 1.1\%$ and $\delta\overline{\omega}/\overline{\omega} = 2.1\%$.

2.2. *Cylinder motion history*

As shown by Coles (1965), the flow state at any fixed set of parameter values depends strongly upon the history of the cylinder motion. For some specific Reynolds numbers, Coles was able to generate up to 26 different flow states. Thus, in order to maintain uniqueness of the flow state, it is important to accelerate the cylinders at a fixed known rate in all experiments. Andereck, Liu & Swinney (1986) found that for dimensional acceleration less than 0.15 rad min^{-2} acceleration effects did not appear to influence the location of transition boundaries. In our facility, this corresponds to $\mathrm{d}Re_{\Omega}/\mathrm{d}t$ of 0.005 s^{-1}. The angular acceleration was conservatively restricted to 0.0015 s^{-1}, that is, a third of the rate suggested by Andereck *et al.* The rate of change of the axial Reynolds number was set to 0.025 s^{-1}. The two stepper motors were driven by separate square wave outputs generated by a computer.

An initial flow state was established as follows. At first, azimuthal rotation was imparted to the system. Once the desired azimuthal Reynolds number Re_{Ω} was reached, the flow was allowed to approach a steady state by holding the rotation rate fixed for approximately 90 viscous time scales (Weisberg 1996) where the viscous time

scale, t_ν, is defined as

$$t_\nu = \frac{d^2}{\nu}, \tag{2.5}$$

and amounts to about 25 min or 375 rotations of the inner cylinder. Axial motion was then imparted. The desired initial axial Reynolds number Re_{ax} (the starting point of the parametric cut) was known beforehand. To find the location of the resonance horns, a one-parameter cut at constant Re_Ω was performed at 16 almost equally spaced intervals in Re_{ax}. The path of increasing Re_{ax} was chosen so as to have a reasonable chance of passing through a wide resonance horn (and thus locate a region of frequency-locking, as will be explained below) and the step-size was chosen to be small, typically $\Delta Re_{ax} = 0.4$, achieved by increasing the axial forcing frequency. A cut that is too 'high' in the resonance horn may enter a chaotic region (as adjacent horns may have interacted) while a cut that is too 'low' may not reveal frequency-locking since the horn in its early stages of growth may not produce signals strong enough to quantify the dynamics present within it. Thus, the cut location and the step-size were chosen through trial and error, as no prior knowledge about the horn development was available. After each settling and data acquisition period, the axial Reynolds number was increased abruptly by 0.4 (the effects of such a small sudden finite change in rotation rate are not known, but are assumed to be negligible) and the settling and data acquisition process was repeated until the parametric cut was complete.

2.3. *Data acquisition and processing*

All the quantitative data were obtained using Kalliroscope flow visualization. The flow was illuminated through a ring lamp placed just above and in front of the outer cylinder. This lamp location produced a slight axial gradient in the grey-scale value of the images. Although this gradient could be reduced by placing a similar light source at the bottom of the apparatus, a significantly reduced light contrast resulted. Since our principal objective was to study the temporal characteristics of the flow pattern, a high degree of contrast was considered to be more important than the slight axial gradient in the image brightness.

All the images were obtained using a Panasonic WV-BD400 CCD camera. The camera, with a resolution of 646×496 pixels, was placed sufficiently far away from the apparatus so that the axial field of view typically covered ten pairs of vortices and so that the image of the outer cylinder was just within the horizontal field of view. This location gave sufficient axial resolution for accurate axial wavenumber measurement and sufficient resolution in the temporal (horizontal) direction. The maximum signal to noise ratio possible was 1024:1 since the CCD camera was a 10-bit camera. The camera was triggered through a square wave. Typical frequencies of interest were about 1–2 times the axial forcing frequency, that is, approximately 0.2 Hz. It was deemed that 50 points per cycle would provide adequate temporal resolution, and the image acquisition rate, f_{grab}, was set to 10 Hz. To resolve the power spectrum, 4096 images were obtained per data point, and so $\Delta f = f_{grab}/N = 0.00244$.

Multiple snapshots of the flow were acquired using a digital frame-grabber card. A one pixel thin central slice was extracted from each snapshot. These were then placed in chronological order to form a 'stack.' The slice extraction process is illustrated in figure 2 and a subsequent sample stack is shown in figure 3.

In each stack, the vertical direction represents axial location and the horizontal direction represents time, since each slice represents the flow pattern at a fixed point in the flow, but separated in time by a small constant time delay of 0.1 s. Because of

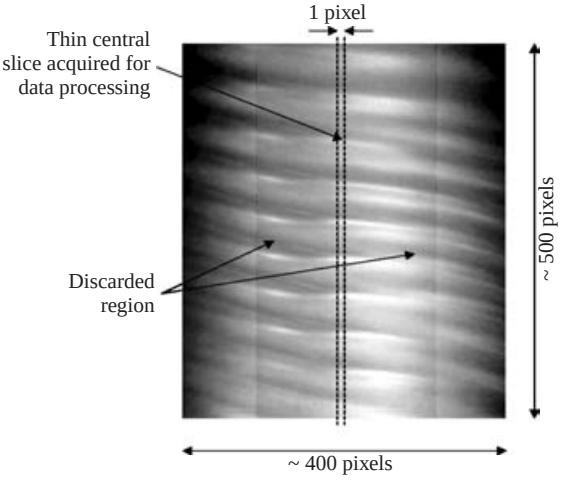

FIGURE 2. Extraction of a thin vertical slice from an individual flow snapshot. The parts of the image on either side of the slice are not used in forming the stack. The 1 pixel wide slice was about 1/50 of the gap width d.

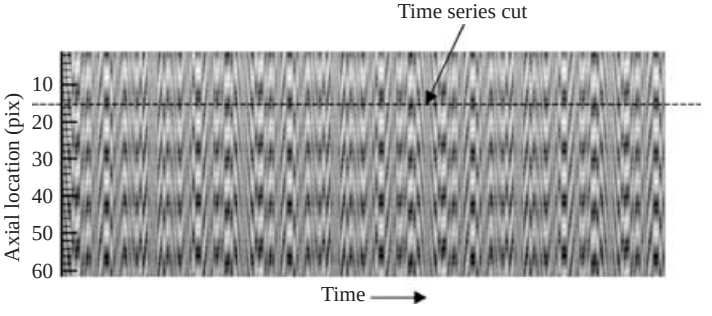

FIGURE 3. A stack formed by chronologically accumulating a thin one-pixel slice from successive flow snapshots over a period of about 90 s or about six forcing periods T_f. Horizontal (temporal) cuts through the stack generate raw grey-scale time series.

the high number of images (about 100 for each forcing cycle), the stack contains high-frequency information on the flow dynamics. A sample stack, obtained for azimuthal and axial Reynolds numbers of 244 and 65.0, respectively, is shown in figure 3.

The time series of the grey-scale value at a fixed physical point in the flow was obtained by extracting a horizontal cut through the stack, corresponding to the dashed line in figure 3. The power spectrum of the time series verified that an axial gradient in the grey scale (originating from the lighting) did not, as expected, affect the temporal properties of the time series. The power spectrum revealed the underlying frequency components, while a phase portrait and subsequently a Poincaré map were constructed. A rotation number plot, illustrating the variation in rotation number along a one-parameter cut through three-dimensional parameter space, was ultimately generated. The rotation number (the ratio of the bifurcation frequency to the forcing frequency) describes the dynamics of the bifurcation (see § 4.4); it is used to identify the existence of frequency-locked regions (resonance horns), the growth of these horns with increasing distance from the critical surface, whether the horns interacted and to consequently identify regions of quasi-periodic flow.

The axial–azimuthal wavenumber development was captured using four Polaroid digital cameras spaced equally around the apparatus. The cameras were triggered simultaneously and the four image segments were concatenated to form a complete surround image. The survey consisted of fixing the azimuthal Reynolds number and increasing the axial Reynolds number. Each value of the axial Reynolds number constituted a single data point. Once the flow had reached steady state at the required axial Reynolds number, ten sets of surround images were obtained at equally spaced values of increasing Re_{ax}. Typically, a step size of $\Delta Re_{ax} = 10$ was chosen. This was repeated for a number of different rotation rates.

In the dynamical study, the region investigated was necessarily small since quasi-periodic transitions appeared to be limited to a relatively narrow region (Marques & Lopez 2000). The increments in Re_{ax} were commensurately small to obtain adequate spatial resolution in locating and identifying the resonance horns. The spatial study of the postcritical spatial behaviour, however, examines a much larger region of parameter space (the entire region above the critical curve in figure 11). The maximum span of Re_{ax} being investigated was approximately 100, and so larger increments in Re_{ax} of 10 were chosen. The postcritical region was mapped out by performing cuts in the direction of increasing Re_{ax} at fixed Re_{Ω}. Along each cut, Re_{Ω} was fixed and Re_{ax} was increased in steps of 10. Once a subcritical flow state had been reached, the cut was terminated. The rotation rate was then increased by a prescribed amount and another constant Re_{Ω} cut was performed. This procedure was continued until the entire postcritical region had been mapped.

The axial wavenumber was determined from a one-pixel thin axial slice of the flow while the azimuthal wavenumber was acquired from the composite surround image. A contour plot of the axial–azimuthal wavenumbers was used to determine whether the wavenumber changed very sharply close to the Neimark–Sacker bifurcation, as was suggested by the analysis of the same flow (Marques & Lopez 2000).

The azimuthal wavenumber near criticality is difficult to determine accurately because the waves on the vortex structures have small amplitude. The axial wavenumber measurement is subject to a number of sources of error. At large Re_{ax}, isolated inhomogeneities may occur and lead to a slight disruption in the axial periodicity. Such images were discarded. Furthermore, near the critical surface, the vortices are weak and only a portion of the axial window may contain vortices of sufficient strength. The vertical extent and corresponding FFT window must be correspondingly reduced to include only axially periodic structures. Finally, three flow snapshots were acquired at random times at any given Reynolds number and used to obtain an average axial wavenumber. This approach assumes that k does not vary with time at a given flow setting and is based on the belief that although the dynamic competition between the forcing and rotation leads to a time-varying fluid transfer between vortex pairs, this does not affect the axial wavelength of the flow structures, merely the growth rate and, hence, the vortex core diameters. (Note: we make measurements only when the Taylor spirals are fully developed, and find that the peak axial wavelength does not exhibit time variations.)

3. Fundamentals of the transition

3.1. *Analysis of the base flow*

The base flow consists of a superposition of steady circular Couette flow (CCF) and time-periodic annular Stokes flow. The fluid motion is thus time periodic (with the period of the forcing) and three-dimensional; we refer to this flow state as helical

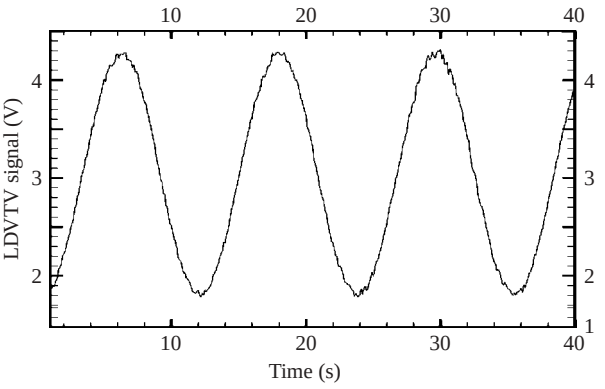

FIGURE 4. Voltage time series from the LVDT obtained over about three forcing cycles.

Couette flow (HCF). In HCF, the streamlines at any instant in time are helical in shape and no vortical structures are present. As the axial flow component increases relative to the rotational component, the helical path becomes less 'compressed.' Although the flow is time-periodic, the Kalliroscope visualization technique shows a flow that appears steady in time since the shear stress distribution is uniform throughout the flow. Note that in the base flow, the signal-to-noise ratio was 1.9 %, which about the upper limit for generating accurate Poincaré maps.

It is important to examine the mechanical precision of the forcing, in particular the temporal 'purity' of the Scotch-yoke forcing mechanism. According to Swift & Wiesenfeld (1984), the precise nature of the temporal forcing can interact with the spatial symmetries present in the system, which in turn determine which bifurcations may or may not take place at any stage. To study this question, the time trace of the forcing motion was studied using a linear variable differential transducer (LVDT) attached to the top of the cylinder. Figure 4 illustrates the voltage time series from the LVDT.

The figure clearly shows that the voltage signal has one dominant frequency component (corresponding to the axial forcing frequency), but that it is not purely periodic. It appears that the axial motion is smoother during the unidirectional parts of the cycle than at the extremes, where the cylinder changes direction of motion. Nevertheless, an analysis of the power spectrum revealed that these signals are small in comparison to the forcing signal; the strength of the first harmonic is only about 2 % of the main forcing signal.

Although this component is very small, its effects on the flow are difficult to predict. Marques *et al.* (2002) consider how bifurcation diagrams and sequences are altered in the presence of small perturbations that affect existing symmetries in the system. The particular symmetry in question is the glide-reflection symmetry. This symmetry, denoted by S, is a reflection about the plane orthogonal to the cylinder axis with a simultaneous time translation of half a period, and satisfies the property $S^2 = I$, since applying the symmetry argument twice in succession leads to a return to the original flow state. According to the results of Swift & Wiesenfeld (1984), if the forcing is not purely harmonic in our system, then this symmetry is broken. If the forcing is purely harmonic, period-doubling bifurcations may not occur as the primary bifurcation. If this particular symmetry is destroyed, however, period-doubling bifurcations may subsequently occur. Marques *et al.* (2002) analysed the bifurcation properties of this system while considering non-harmonic axial oscillations

of the form $W(\sin\omega_f t + \epsilon \sin 2\omega_f t)$ where ϵ is a measure of the imperfection of the forcing. Their preliminary results suggested that with $\epsilon = 0.02$ the bifurcation diagrams did in fact change, and in particular, certain branches lost symmetry while other regions (in which specific dynamical structures existed) grew or reduced in size. Their value of ϵ, 0.02, is (coincidentally) the same as that observed in this facility, and so it may be that imperfections in the driving signal will have some small (though unquantifiable) effect on the dynamics observed in the experiment.

3.2. *Measurement of the transition Reynolds number*

The measured transition Reynolds number depends on the particular detection analysis technique employed. According to Benjamin & Mullin (1981), the first transition is sudden in an infinite aspect ratio system, but gradual in a finite aspect ratio system, where Eckman cells (of the order of the gap width) exist at the endwalls for all non-zero rotation rates. The rest of the annulus may be considered to be (at least approximately) two-dimensional. As the rotation rate is increased, the first visual appearance of Taylor vortices typically occur below the theoretical critical value. In the experiments of Cole (1976), Taylor cells first appeared at speeds as low as 70 % of the expected critical rotation rate. The cells generally form at the endwalls and progress toward the centre of the test section with increasing rotation rate. Cells may also be seen at sporadic locations elsewhere in the annulus.

The method used in this study was identical to that used by Weisberg *et al.* (1997). A central axial strip was captured and digitized at each rotation rate, and the standard deviation, σ, of the axial grey cale distribution was found. This procedure was repeated from subcritical to supercritical rotation rates, in increasing and decreasing directions. The standard deviation was then plotted against rotation rate and a curve fit obtained for the data. The curve fit was of the form $\sigma = A + B\tanh((Re_\Omega - C)/D)$ and the constants A, B, C and D were determined through a least-squares error analysis. The critical rotation rate was defined as the rotation rate at which the slope of the curve, $\mathrm{d}\sigma/\mathrm{d}Re_\Omega$, was maximum, that is, at the (only) point of inflection of the curve. Via this method, $Re_{\Omega,crit} = C$.

In Weisberg's study, the primary transition is between an axially uniform flow and a flow with axial periodicity, as it is in the present work. Our flow, however, differs in one crucial respect. A dynamic competition exists between the axial and rotational cylinder motions: the azimuthal rotation encourages Taylor cell growth while the axial oscillation suppresses them. Thus, the instantaneous vortex growth rate depends upon the relative magnitudes of the two Reynolds numbers. While the actual transition Reynolds number does not depend on this ratio, the visual observation of vortices does: even beyond criticality, vortices will not be seen unless their growth rate is large enough so that they are visually prominent. The structures must have grown for a sufficiently long time in order to be visible. Thus, to be consistent, snapshots of the flow were obtained and their corresponding axial standard deviations calculated at the point of zero instantaneous forcing amplitude, that is, at the extremum of the forcing, when Re_{ax} is instantaneously zero.

3.3. *Character of the primary transition*

The primary transition can be subcritical or supercritical. Subcritical transitions are hysteretic while supercritical transitions are not. Hysteretic transitions are more difficult to measure experimentally owing to the influence of the experimental path on the transition Reynolds number. In the absence of forcing, the primary transition to regular axisymmetric Taylor cells is known to be supercritical. In the axially forced

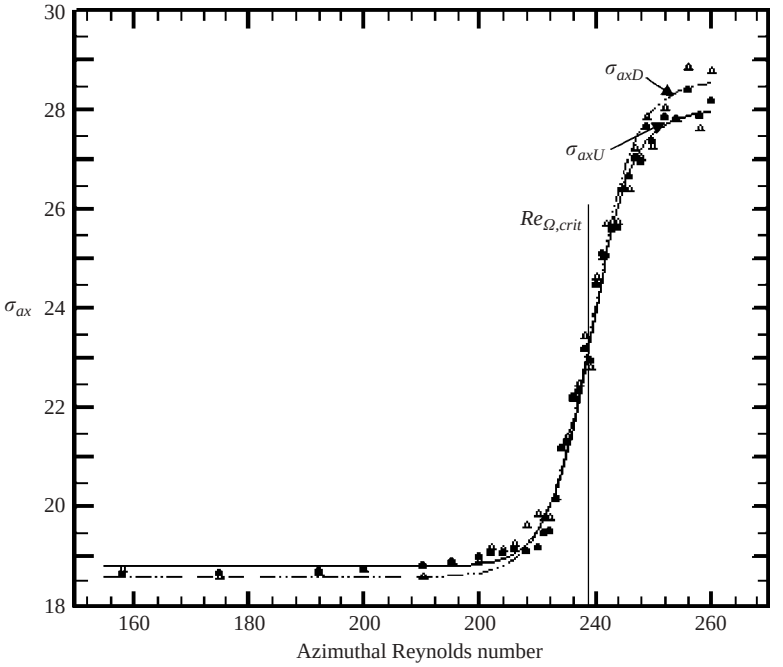

FIGURE 5. Axial grey scale standard deviation σ_{ax} versus azimuthal Reynolds number Re_Ω. Rotation rate ●, increasing; △, decreasing. ———, $\sigma_{axU} = 23.4 + 4.60\ \tanh((Re_\Omega - 239.00)/7.5)$; —··—··—, $\sigma_{axD} = 23.6 + 5.00 \tanh((Re_\Omega - 239.04)/8.0)$. The essentially equal upward and downward transition values confirm this transition to be supercritical.

case, the character of the base flow is spatially and temporally different and it is unclear how this affects the nature of the primary transition.

A procedure similar to that used to measure the critical rotation rate was employed. The azimuthal Reynolds number was increased in steps of one from a value below criticality to a value above criticality, corresponding to passage through a complete transition. The azimuthal Reynolds number was then reduced to the starting value.

Figure 5 illustrates the standard deviation measurements for increasing and decreasing rotation rates. Prior to the formation of any vortices, the standard deviation is essentially constant and equal to approximately 18.8. At $Re_\Omega \approx 220$, the standard deviation begins to rise, with the main increase occurring at $Re_\Omega \approx 230$. At this point, wavy vortices are just visible at random locations in the flow and small increases in rotation rate produce measurable changes to the strength of the vortices. At $Re_\Omega \approx 245$, the curve starts to flatten out, essentially becoming constant at about 250. At this value of Re_Ω, the entire annulus is filled with vortices and growth of the vortices has ceased.

The critical Reynolds number was found to be 239.0, which agrees with the theoretical Floquet value of 244.0 given by Marques & Lopez (1997) to within about 2 %. The r.m.s. uncertainty in $Re_{\Omega,crit}$ is 0.72 % which, based on a transition Reynolds number of 244.0, gives an uncertainty of $\Delta Re_{\Omega,crit} = 1.74$. This estimate incorporates only contributions due to random errors; systematic errors (such as mechanical vibration, eccentricity effects, and non-harmonicity of forcing), which are difficult to account for, will increase the uncertainty in the measurements.

According to figure 5, the critical rotation rate in the increasing and decreasing directions is 239.0 and 239.04, respectively, that is, they are equal to within

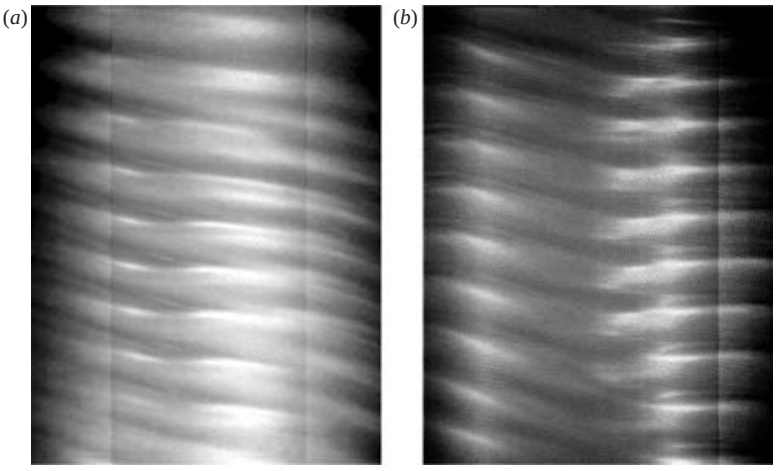

FIGURE 6. Flow snapshots of Modes I and II, respectively, for slightly postcritical Reynolds numbers. (*a*) Mode I; $Re_{ax} = 79$, $Re_{\Omega} = 247$. (*b*) Mode II; $Re_{ax} = 91$, $Re_{\Omega} = 280$.

experimental error. Apparently, the primary transition occurs without hysteresis and is thus supercritical in nature. This observation may be partly explained by considering the base flow. In the unforced case, the base flow is purely azimuthal while in the forced case it also has a time-periodic axial component. The two components, however, essentially superpose prior to the primary bifurcation, at least with regard to their effect on the nature of subsequent transitions. The transition in the forced and unforced cases is driven by the inner cylinder rotation destroying the radial force balance. The presence of a time-varying axial component should not affect this radial force balance. Thus we think of the base flow as the superposition of classical Couette flow, which has a supercritical primary transition, and a time-varying Poiseuille flow which does not undergo any transition in this parameter regime. Since only the Couette flow component undergoes a transition, the nature of its transition should be the determining factor. Furthermore, with the primary transition being supercritical, the location of the transition surface and the sought-after resonance horns are not expected to depend upon the actual parametric path chosen and so we are free to use any path we desire.

3.4. *Flow snapshots and comparisons to the unforced case*

Snapshots of the flow at slightly postcritical and highly postcritical Reynolds numbers are shown in figures 6 and 7. The qualitative flow structure changes drastically as the rotation rate rises beyond the critical rotation rate. Two different flow states, which we refer to as Mode I and Mode II, are shown, corresponding to the points indicated in figure 9. Figure 6 is for a slightly postcritical rotation rate ($1.05Re_{\Omega,crit}$) while figure 7 is for a highly postcritical rotation rate ($1.50Re_{\Omega,crit}$). Both modes consist of inclined wavy Taylor cells. Mode I contains one azimuthal wave per vortex spiral while Mode II contains two waves per spiral (observed from surround 360° views). Typically, Mode I exhibits larger axial wavelength and the maximum spatial inclination of the spirals is less than in Mode II. The random visual defects visible in figure 7 are due to interactions between individual vortex spirals.

As the rotation rate increases, the waviness appears abruptly at local points in the flow. As mentioned previously, the critical rotation rate is defined as the rotation rate at which the growth rate of axially periodic structures, or specifically the axial

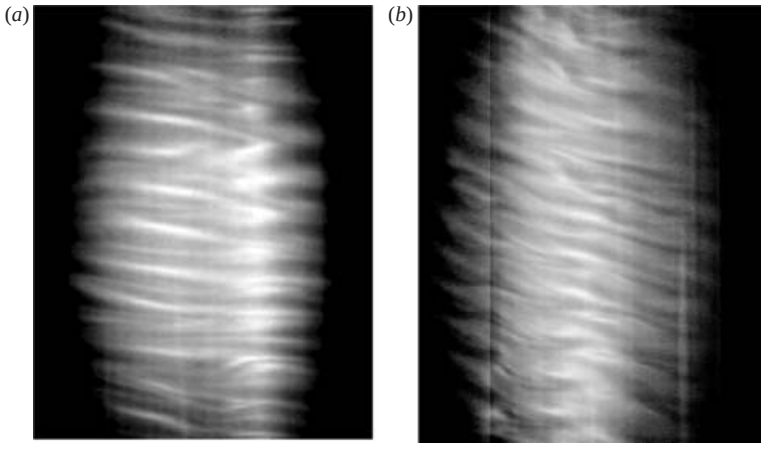

FIGURE 7. Flow snapshots of Modes I and II, respectively, for highly postcritical Reynolds numbers. (*a*) Mode I; $Re_{ax} = 79$, $Re_{\Omega} = 280$. (*b*) Mode II; $Re_{ax} = 91$, $Re_{\Omega} = 320$.

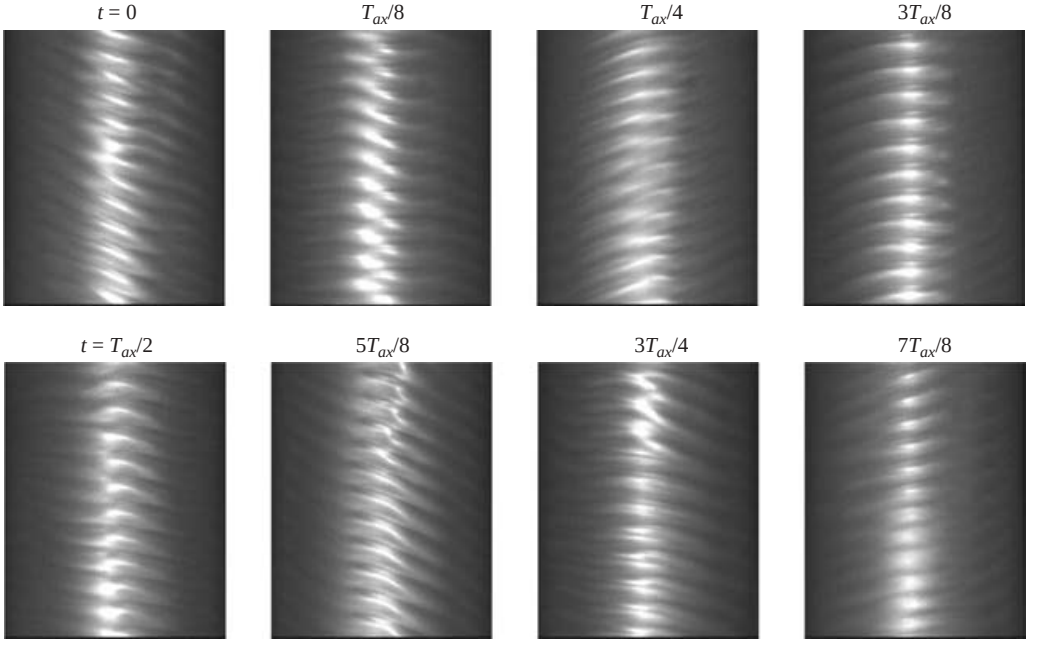

FIGURE 8. Snapshots of the bifurcated flow in Mode I separated by equal time intervals. Eight snapshots are shown over one complete axial forcing period for flow parameters $Re_{ax} = 79$ and $Re_{\Omega} = 250$.

grey scale standard deviation, has reached a maximum value. Owing to the dynamic competition between the azimuthal rotation and axial oscillation, the instantaneous flow structure varies with time for a given set of (Re_{ax}, Re_{Ω}). The maximum time rate of growth of the Taylor cells occurs when the instantaneous forcing amplitude is zero, that is, at the extrema of the forcing, since the axial oscillations suppress Taylor cell growth. Thus, during the early stages of mode formation, vortical structures are not initially visible throughout the entire forcing cycle; a higher rotation rate is necessary to overcome this damping. Figure 8 illustrates the evolution of the Mode

I flow state at eight periodic intervals during a single forcing period. Owing to the frequency-locked nature of the flow, the specific phase of the cycle in the figure is not important; the flow will eventually repeat (with a period greater than the forcing period T_{ax}).

The point when the growth rate of the vortical structures reaches a maximum value coincides, in practical experience, with the vortical structures essentially being visible for all time. The increase in rotation rate from when the point vortices are first seen to the point of complete vortex formation is larger for Mode II; this is probably due to the larger forcing amplitude involved and hence the relatively shorter time available for the waviness in Mode II to grow to a sufficiently large amplitude. Within one complete forcing period, the instantaneous inclination of the Taylor structures also varies with time. The maximum inclination, with respect to the horizontal, occurs when the forcing amplitude has reached its maximum instantaneous value, corresponding to the mid-point of the axial oscillation. The waves occur at the same azimuthal position in all vortices and travel in phase with one another.

The physical vortices are defined by a vortex core size and a core-to-core separation; both parameters are measured from the axial grey-scale distribution. The core-to-core separation is defined as the axial wavelength of the grey-scale distribution. The vortex core size is obtained by examining a plot of the axial grey-scale distribution; the edges of the vortex core are defined by points where the Kalliroscope flakes are 'edge-on' to the camera, that is, the grey-scale image reveals a dark edge. Note that while the conclusions made in the present work do not require quantitative measurements of the vortex core size and a core-to-core separation, these concepts are useful in comparing the various flow states in a qualitative manner.

The vortex core size and core-to-core separation vary azimuthally and temporally for a fixed point in the flow. This arises because of the time-variation in instantaneous forcing amplitude, which results in a cyclically varying growth rate driving both length scales. While the character of the transition, that is, its supercritical nature, is identical to that in the unforced case, the spatial development of the flow structure beyond the primary bifurcation differs greatly. In the unforced case, a sequence of well-defined transitions occur that lead to stable structures with increasing degrees of spatio-temporal complexity. However, the structures are still very regular and ordered (at least up to 10 times the critical rotation rate). In the forced case, this is not so. A relatively small increase in the rotation rate beyond the primary bifurcation leads to a rapid loss in flow regularity manifested by a complete and gradual loss in axial and azimuthal periodicity. Local regions of regular waviness develop and these become separated by regions of random waviness and chaotic flow. In the axial direction, it appears that random vortex deformations and interactions regularly occur, as is evident in figure 7. In effect, the axial forcing appears to destabilize the non-axisymmetric wavy modes, as suggested by Marques & Lopez (2000).

4. Analysis of temporal dynamics

4.1. *Two-dimensional projection of critical surface from numerical simulations*

The Floquet analysis of Marques & Lopez (1997) showed that, except for a small window in parameter space, $n = 0$ is generally the most unstable azimuthal mode in the presence of axial forcing (n being the azimuthal wavenumber). Generally, the primary bifurcation leads to an axisymmetric mode that is synchronous with the forcing, so that no new frequencies are introduced via the bifurcation. However, within this small window (restricted to small $\overline{\omega}$ and large Re_{ax}), the $n \neq 0$ modes

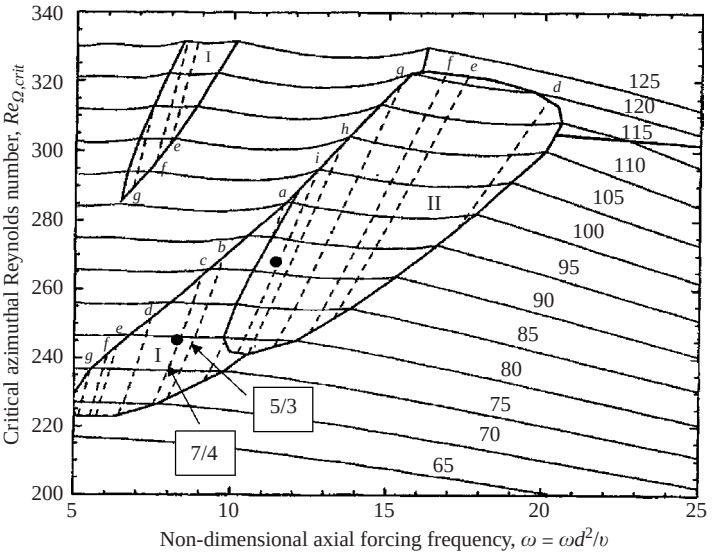

FIGURE 9. Critical rotation rate as a function of non-dimensional forcing frequency. Thick solid lines separate different azimuthal modes and marked contours (65–125) are for fixed Re_{ax}. Dashed lines indicate the tip locus of the horns from where strong temporal resonances (with $\omega_s/\omega_f = p/q$) emanate (ω_s is the secondary bifurcation frequency, and p and q are integers). Resonance horns 5/3 and 7/4 in Mode I were investigated in detail. Labels a to i refer to strong resonances 3/2, 5/3, 7/4, 2/1, 9/4, 7/3, 5/2, 8/3 and 11/4. (Reproduced with permission from Marques & Lopez 2000).

are most unstable and, simultaneously, a new frequency (ω_s) is introduced into the dynamics of the system. This means that ω_s and ω_f are now both required to describe the observed dynamics.

The method used to determine the value of ω_s assumes that the dynamics can be fully explained by two independent frequencies and the observed power spectrum (a sample of which is shown in figure 13). By testing how each dominant peak (these have been labelled) can be expressed in terms of a linear combination of ω_f and ω_s, the values of ω_f and ω_s are determined in a straightforward manner.

These primary bifurcations occur for $Re_{ax} \geqslant 68$ and ω in between the natural frequencies of the unforced spiral modes; typically $\overline{\omega} \sim O(10)$ (Marques & Lopez 2000). Figure 9 shows the critical surface projected onto the $(\overline{\omega}, Re_{\Omega,crit})$-plane; the dark lines define bounded islands where the $n \neq 0$ modes are most unstable. Visualizations of Modes I and II were obtained within these islands at the points shown by the black dots in the figure. We pay particular attention to the Mode I flow dynamics in the vicinity of the 5/3- and 7/4-resonance horns.

The flow modes are described by an integral azimuthal wavenumber n and a (generally) non-integer axial wavenumber k. As described earlier, the axial wavelength λ of the spiral vortices is obtained from the axial grey-scale distribution. The axial wavenumber is defined as $k = 2\pi/\lambda$. The primary critical surface shown in figure 9 was obtained by numerically determining which (n, k) mode was most unstable for a given $(Re_{ax}, \overline{\omega})$, that is, which mode bifurcated at the lowest rotation rate. Outside the regions labelled I and II the primary bifurcation was axisymmetric and synchronous with the forcing. Inside regions I and II the primary bifurcation was non-axisymmetric, and a pair of complex conjugate eigenvalues, related to the linearization of the solution

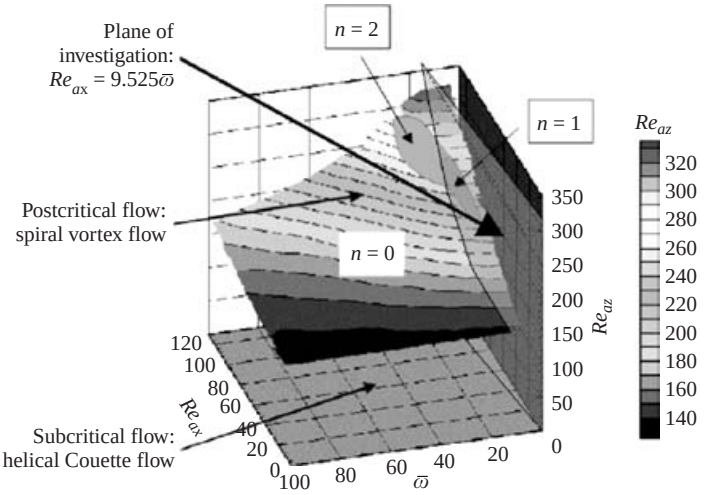

FIGURE 10. Slicing the primary critical surface (obtained from data contained in Marques & Lopez 2000) with the plane of investigation ($Re_{ax} = 9.525\overline{\omega}$). The result is a critical curve in this plane. As shown, the selected curve passes through the $n = 1$ region and just misses the corner of the $n = 2$ region.

losing stability and to the resulting bifurcated dynamics, simultaneously crossed the unit circle as Re_{Ω} was raised. This leads to a Neimark–Sacker bifurcation where quasi-periodic and frequency-locked flow states arise. While figure 9 indicates the extent of the critical surface, what temporal resonances (defined by the rotation number ω_s/ω_f) can be expected, and from which points on the critical surface the resonance horns emerge (that is, the tip locus of the horns), it does not indicate the shape and size of the resonance. This information must be provided by experiment.

4.2. *Reconstruction of the three-dimensional primary critical surface*

Figure 9 illustrates the projection of the critical surface onto the $(\overline{\omega} - Re_{\Omega,crit})$-plane. When viewed in three dimensions, the critical surface appears as in figure 10. The critical surface is curved and slopes in parameter space. The critical rotation rate increases with axial forcing amplitude and decreasing forcing frequency (the latter increases the influence of the axial oscillations by increasing the extent of the oscillatory Stokes layer). The portion of the critical surface where non-axisymmetric modes bifurcate is only about 2 % of the total critical surface area illustrated in figure 10. This supports the general consensus that such observations are rare in fluid mechanical systems. Above the enclosed regions indicated by $n = 1$ and $n = 2$ lie the frequency-locked and quasi-periodic regimes being investigated.

In our apparatus, Re_{ax} and $\overline{\omega}$ are not independent but linearly coupled, although the constant of proportionality can be changed discretely to allow independent explorations of Modes I and II. The observations presented here are, however, all focused on Mode I, and we are restricted to the vertical plane $Re_{ax} = 9.525\overline{\omega}$. The result of this intersection is a curve in two dimensions denoted by the thick black line in figure 10.

Figure 11 illustrates the critical curve projected onto the (Re_{ax}, Re_{Ω})-plane, that is, when projected onto the dark vertical plane in figure 10. Below this curve, the base flow is helical Couette flow (HCF). Above the curve, the bifurcated flow structure will, for a given cylinder motion history, depend on the magnitudes of the axial

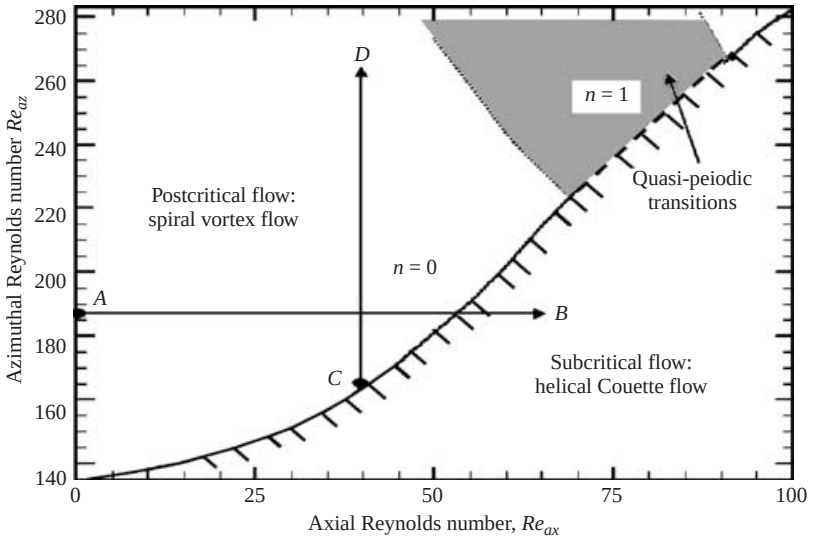

FIGURE 11. Critical curve obtained by slicing the critical surface (reproduced from Marques & Lopez 2000) with the vertical plane of investigation. The shaded $n = 1$ region emanates from the island labelled $n = 1$ in figure 10 and that is where the temporal investigations are focused.

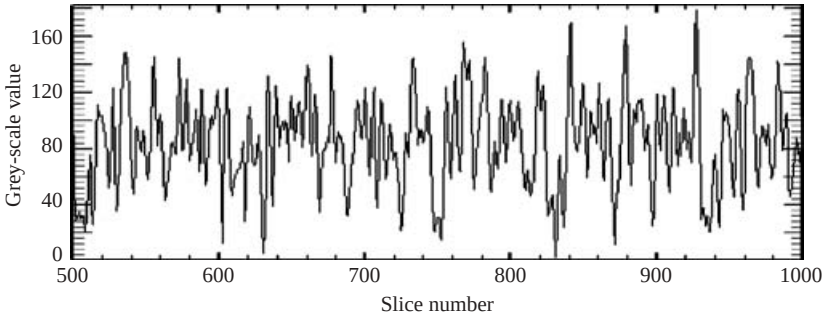

FIGURE 12. Part of the time series of the grey-scale intensity at a fixed point in the flow for the parameters (65.0, 244). The time period between successive slices is 0.25 s and the time series lasts for about 120 s.

and azimuthal Reynolds numbers. In the shaded region we expect to find transitions leading to quasi-periodic and frequency-locked flow states (the boundaries of the shaded region are schematic only, since they are not known *a priori*). Our objective is to search for resonance horns within this region by performing multiple high-resolution cuts throughout the shaded region, each at a different fixed Re_Ω. Although the regions labelled $n = 1$ and $n = 2$ are schematic only, their presence is useful in that it provides an illustration of their shape and size and how they relate to the plane of investigation.

4.3. *Sample results for* ($Re_{ax} = 65.0$, $Re_\Omega = 244$)

The point ($Re_{ax} = 65.0$, $Re_\Omega = 244$) corresponds to a location on the inside edge of the 7/4-resonance horn. Typical time traces of the grey-scale intensity with time, power spectra, phase portraits and Poincaré maps are shown in figures 12 to 15.

The time trace corresponding to (65.0, 244) is shown in figure 12, and the spectrum (figure 13) shows many peaks. The first nine peaks have been identified as comprising

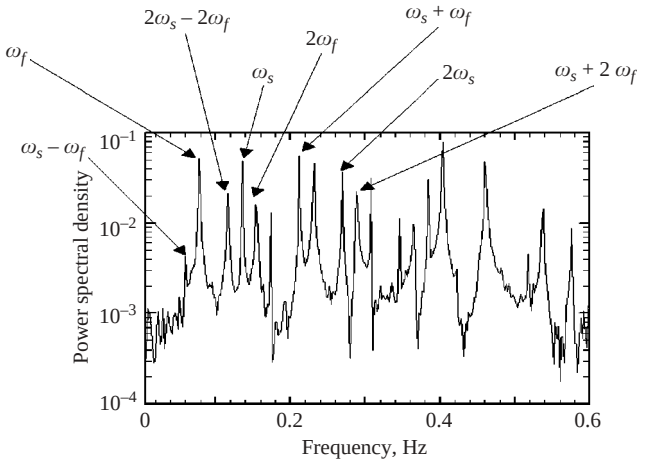

FIGURE 13. Power spectrum of the time series obtained for the point (65.0, 244). The significant spectral peaks can be identified clearly as linear combinations of the forcing frequency ω_f and bifurcating frequency ω_s.

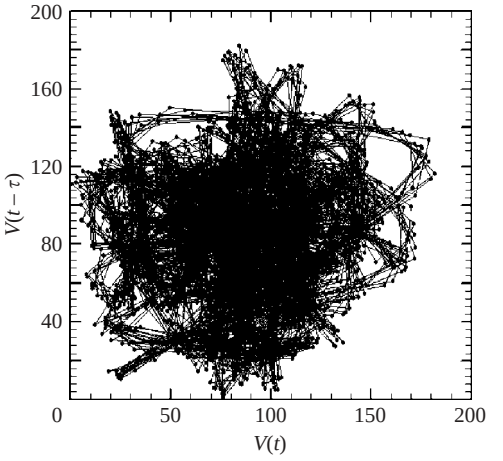

FIGURE 14. Phase portrait of the light intensity $V(t)$ and the delayed light intensity $V(t-\tau)$ projected onto the $(V(t), V(t-\tau))$-plane, constructed from the time series for a point in the 7/4-horn.

the forcing and bifurcating frequencies (and their harmonics), and linear combinations of the two. The amplitudes vary considerably, and the contributions from other sources such as background noise cannot be readily identified. Although not shown, the time series for subcritical flow showed little noise (less than 0.5 % of the mean level) around a constant grey-scale level, as no vortical structures were present in the flow.

A simple technique for producing phase portraits and Poincaré maps in experimental work is to use 'delayed coordinates' (Packard *et al.* 1980; Takens 1981) to generate one or more time series from an original time series which is useful when two or more independent quantities are not available. Figure 14 is a two-dimensional delay reconstructed phase portrait projection of the time signal. Here, $V(t)$ is the original light intensity at one point in space and $V(t-\tau)$ is the time-delayed signal; thus only one time-delayed signal is used here. The time delay, τ, for these data is

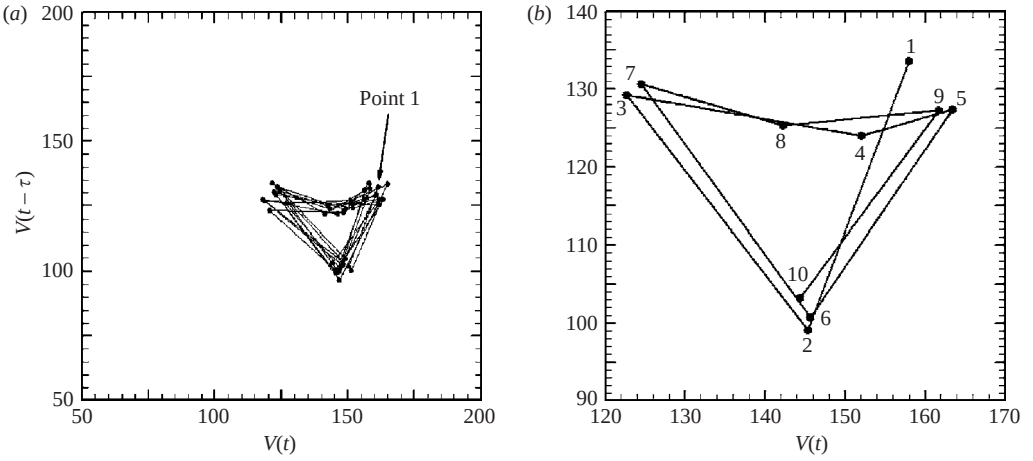

FIGURE 15. Poincaré map for the frequency-locked phase portrait in figure 14 (with almost the same time delay as in figure 14.) In (*b*), the first ten points only are shown. In (*a*), the projection of all intersection points (obtained by periodically strobing the entire phase trajectory) onto the plane of projection is also represented.

$T_f/10$ where T_f is the forcing period. The particular fraction of the forcing period used for the delay (in this case a tenth) that generates the clearest phase portrait and Poincaré map is a function of signal quality and duration and must be determined partly by trial and error.

Each pair of points (from the original and time-delayed series) constitutes one point on the phase portrait. Successive points have been joined together so as to suggest time evolution on the portrait.

Figure 14 represents the projection of the phase portrait onto the $(V(t), V(t-\tau))$-plane. The figure shows the timewise evolution of the portrait over an interval of approximately 40 forcing periods. Many of the points appear to lie inside a vaguely defined central 'cluster'. The phase trajectory typically spends most of the time inside the cluster region, but occasionally 'comes out' for a very brief period before re-entering. While it is difficult to see from the figure, it appears the phase trajectory weakly precesses about a central core. Approximately 50 % of the points are situated inside the tube-like cluster, which provides an indication of the time the trajectory spends there.

In order to generate Poincaré maps, we periodically strobe the phase trajectory every forcing period. Because of the harmonic nature of the forcing, strobing the phase trajectory with the period of the forcing becomes equivalent, in this particular case, to extracting the values on the phase trajectory whenever the instantaneous axial Reynolds number reaches a particular fixed value. A sample Poincaré map is shown in figure 15. The map is not for precisely the same data as shown in figure 14, but since the time delays used in figures 14 and 15 are very similar and we are not close to a bifurcation point, the observed dynamics are expected to be very similar.

Because the Poincaré map uses only about 1 % of the number of points in the phase portrait, the underlying dynamics are often clearer. In this case, the Poincaré map reveals the existence of four isolated clusters. Although we may expect to see well-defined points instead of clusters, the noise in the signal prevents a more precise collapse. The trajectory of the strobed signal is nevertheless clear. It performs

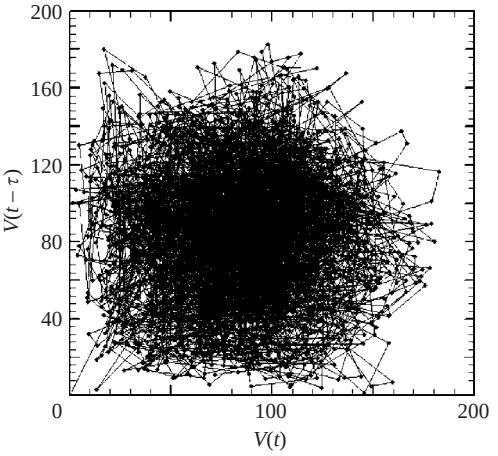

FIGURE 16. Phase portrait, projected onto the $(V(t), V(t-\tau))$-plane, constructed from the time series for a point believed to reside in the quasi-periodic regime.

clockwise loops, successively going from one cluster to the next, which is consistent with the phase portrait.

A key feature of the Poincaré map is the systematic ordering of the points. As may be seen in figure 15, the points labelled 1 to 10 chronologically trace out a clockwise looping pattern. A range of time delays, from $T_f/5$ to $T_f/20$, were investigated. In some cases even shorter time delays were necessary since the clarity of the Poincaré sections was sensitive to the choice of time delay. Typically, time delays of about $T_f/12$ produced the clearest indication of orderly structure. This trial-and-error approach to finding the optimum time delay is required for two reasons: (i) the estimate of the forcing frequency ω_f (and hence strobing period) is subject to error; (ii) the strobing period (even if known precisely) will generally not span an integral number of data points, so that interpolation must be used to calculate the strobed value. A typical grey-scale time series (figure 12) shows that the jump in grey-scale between any two consecutive data points can be quite large: 50 is a typical value, whereas jumps as high as 100 have been recorded often enough to be significant.

Figure 16 shows the results for a flow state believed to represent a quasi-periodic attractor. A slight difference from the frequency-locked trajectory of figure 14 is that this quasi-periodic trajectory does not display as clear a looping path, and the central cluster region appears more diffuse. The apparently quasi-periodic trajectory does not display the clear orbits or precessions evident in the frequency-locked portrait. Instead, the projection appears to display a degree of 'axisymmetry', or lack of directional preference.

4.4. *Calculation of rotation number*

The power spectrum and Poincaré map are both required in order to compute the flow rotation number, defined as ω_s/ω_f. Depending on whether the Poincaré section shows clustering (suggesting frequency-locking) or no clustering (suggesting quasi-periodicity), the method used to compute the rotation number is different.

Since the forcing frequency is known, peaks corresponding to this frequency and its harmonics may be readily identified. The problem arises in identifying the bifurcation frequency. The Floquet analysis predicts the rotation number at any point on the

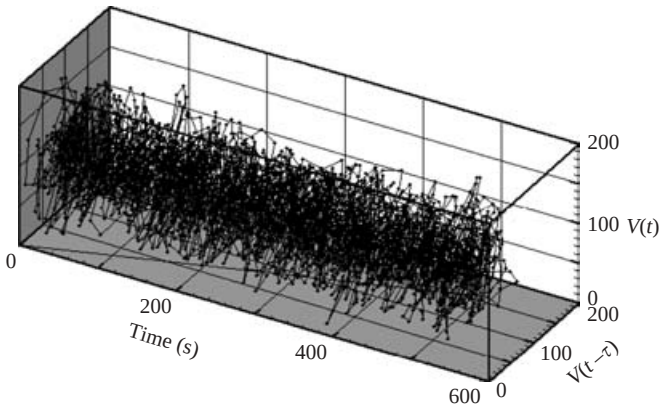

FIGURE 17. Phase portrait for a quasi-periodic state.

critical surface (figure 9). Above the critical surface, however, the rotation number is unknown, although the existence of resonance horns that emanate from special points on the surface is established. Consider, for example, the 7/4-horn. If four clusters are identified in the Poincaré map, the rotation number $\omega_s/\omega_f = p/q$ must be such that $q = 4$, that is, the number of clusters is equal to the denominator of the ratio p/q. When $q = 4$, we may be near the 7/4-horn. If the spectrum has a peak at $\omega = (7/4)\omega_f$, then we may be situated in the 7/4-horn. In addition, if significant peaks in the power spectrum can be expressed as linear combinations of ω_s and ω_f, then the correct rotation number has been found.

If the Poincaré section does not reveal isolated clusters, we do not expect to have frequency-locking (at least as far as we can tell with a signal of our quality, which possesses a signal:noise ratio of approximately 500:1). Instead, we are either in a chaotic regime (far above the critical surface beyond the breakup of the T^2) or in a quasi-periodic regime where the T^2 is still intact, but where ω_s/ω_f is 'practically' irrational. In either case, the lack of visible structure means that the Poincaré section is not helpful in determining the rotation number, and only the power spectrum can be used. If we are in a quasi-periodic regime, we expect that we must be located in the region between adjacent frequency-locked resonance horns of known rotation number (Bergé *et al.* 1984), and we know the range within which the frequency ω_s must lie. The ratio ω_{peak}/ω_f is calculated for the peaks close to the forcing frequency peak. When the value of ω_{peak}/ω_f is equal to a value within the allotted range, we take that value to be the rotation number.

If the experiment were noise-free or had very little noise, the Poincaré section for a quasi-periodic attractor would reveal a closed ring. Figure 17 represents the three-dimensional trajectory of the grey-scale value with time; the projection of this trajectory onto the $(V(t), V(t-\tau))$-plane, that is, its Poincaré map, is shown in figure 16. The figure reveals a cluster with no structure that is more suggestive of a random phase trajectory, as if the data come from the strobing of a chaotic attractor. However, it is our belief that these data actually represent a quasi-periodic attractor and the lack of structure is because of the presence of experimental noise. For example, because of small but measurable temperature fluctuations, the viscosity is continually changing with time, and the three primary dimensionless parameters move within a small three-dimensional volume during the data acquisition process. As a result, the dynamics are continually changing, drifting slightly with time. Within

the resonance horns, this is not a problem (as long as we are not close the edge of the horn) since the flow responds to the changing parameters in such a way as to keep the rotation number fixed (the dynamics are 'locked'). Thus, within a resonance horn, a small 'wandering' of parameters is acceptable. Outside the resonance horn, however, any small wandering will alter the temporal characteristics of the flow since we are effectively sampling a set of different flows, each with its own rotation number. It is conceivable that this sampling could manifest itself as the introduction of appreciable noise on an otherwise quasi-periodic attractor; enough noise, perhaps, to mask the expected ring-like appearance of the strobed section.

4.5. *Power spectra and Poincaré sections from a parametric cut*

To determine how the dynamics evolve above the critical surface, parametric cuts at fixed Re_Ω were performed. At each of the 16 points (along increasing Re_{ax}), a power spectrum and Poincaré map were generated. The rotation number at each point was then calculated and plotted against position in parameter space to reveal the spatial development of resonance horns. Figures 18 and 19 illustrate the results for a parametric cut at $Re_\Omega = 244$. A similar cut at $Re_\Omega = 246$ was also performed, but for brevity its sequences are not shown (see Sinha 2003 for further details).

While the relative strengths of the peaks in the power spectrum are seen to change with forcing amplitude, changes in the Poincaré section typically provide more information. Consider the variation with Re_{ax}. At $Re_{ax} = 65.0$, the Poincaré trajectory consists of four clusters with about a 5 % scatter in each. The plot, coupled with the power spectrum, reveals the rotation number at this point to be rational and equal to 7/4. At $Re_{ax} = 65.4$, the clusters have become more spread out and two of the clusters have almost merged into one; some of the organization evident at $Re_{ax} = 65.0$ is missing while a closed loop characteristic to the map is retained. At $Re_{ax} = 65.8$, drastic changes result. The isolated clusters have disappeared and all organization has been lost. Tracking the location of the peaks at ω_f and ω_s in the spectral plot, the rotation number is calculated to be approximately 1.73. This is 'experimentally' irrational (or a high-order rational such as 173/100) and, bearing in mind the potential effect of noise on quasi-periodic sections, the attractor at this point is believed to be a quasi-periodic T^2. This type of section topology continues until $Re_{ax} = 66.6$. Tracking the rotation number, we see that it reduces to a value of 1.67 when $Re_{ax} = 66.6$. This value is very close to the next low-order rational (5/3), but the large degree of disorder prevalent in the Poincaré section is taken to indicate that the point does not lie within a resonance horn. Then, at $Re_{ax} = 67.0$, substantial organization is seen to return. Three individual clusters can be identified. Via the measured location of the spectral peaks, the rotation number is calculated to be 5/3. Thus, it appears that we have passed through a quasi-periodic regime (beyond the 7/4-resonance horn) and the smaller resonances it contains, and entered the adjacent frequency-locked 5/3-horn. Moving further into the horn, at $Re_{ax} = 67.4$, the Poincaré section topology is clearer. The presence of three compact clusters is striking, confirming that we are still within the 5/3-horn. To within the uncertainty introduced by the step size in Re_{ax} ($\Delta Re_{ax} = 0.4$), the resonance horn edge exists at $Re_{ax} = 68.6$.

The Poincaré sections at Re_{ax} of 67.8, 68.2 and 68.6 do not display as clear an ordering as at $Re_{ax} = 67.4$. The clusters have become more spread out. Tracking the point-to-point movement on an individual section helps to clarify the topology when the clusters begin to spread out. The ratio ω_s/ω_f is still locked at 5/3 in

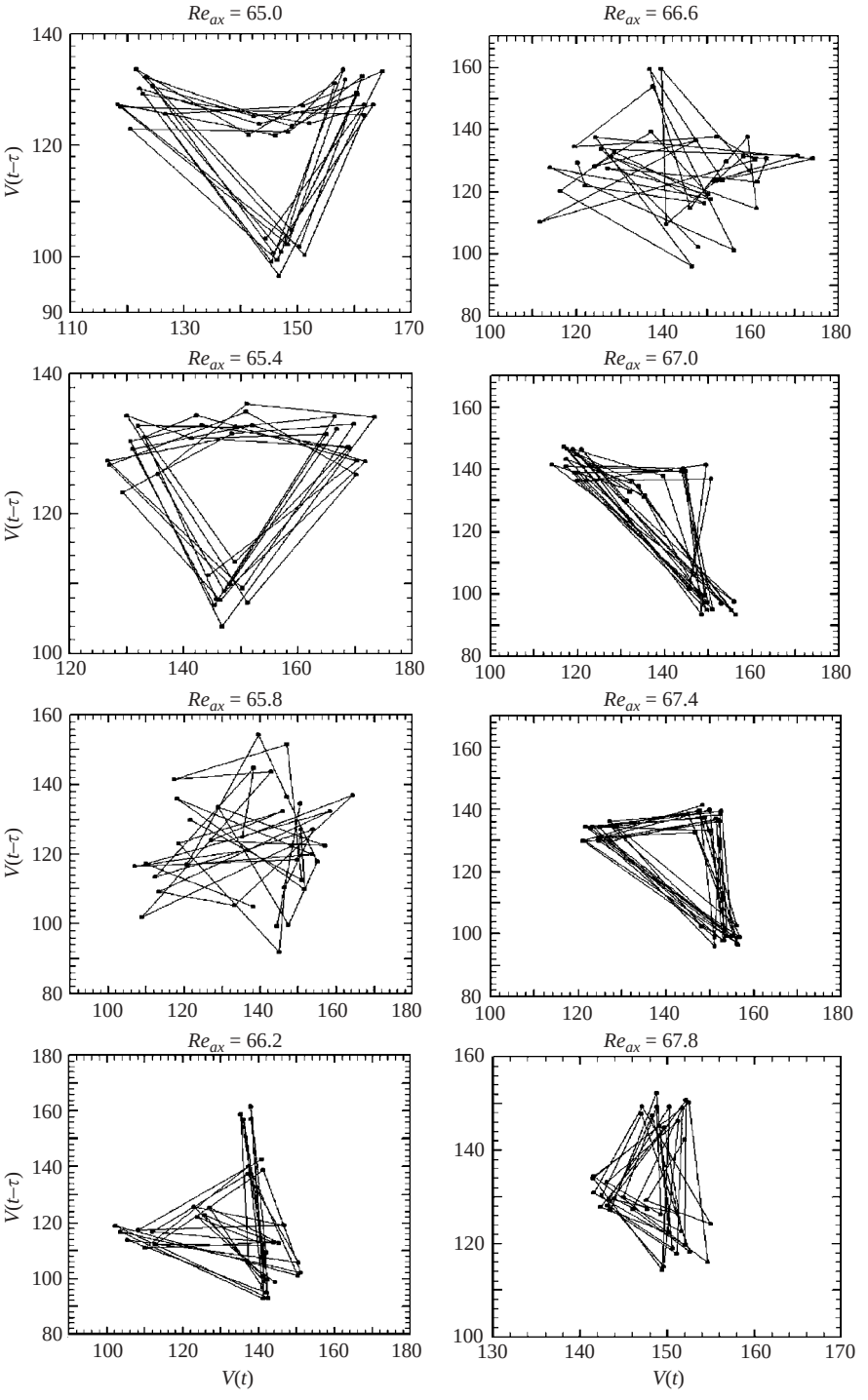

FIGURE 18. Poincaré maps for $Re_{ax} = 65.0$ to 67.8, at constant $Re_{\Omega} = 244.0$.

the power spectrum and so we have enough evidence to label these points as lying within the 5/3-horn. At $Re_{ax} = 69.0$, disorder and a lack of clustering suggest that we have crossed through the 5/3-horn and have entered another quasi-periodic regime.

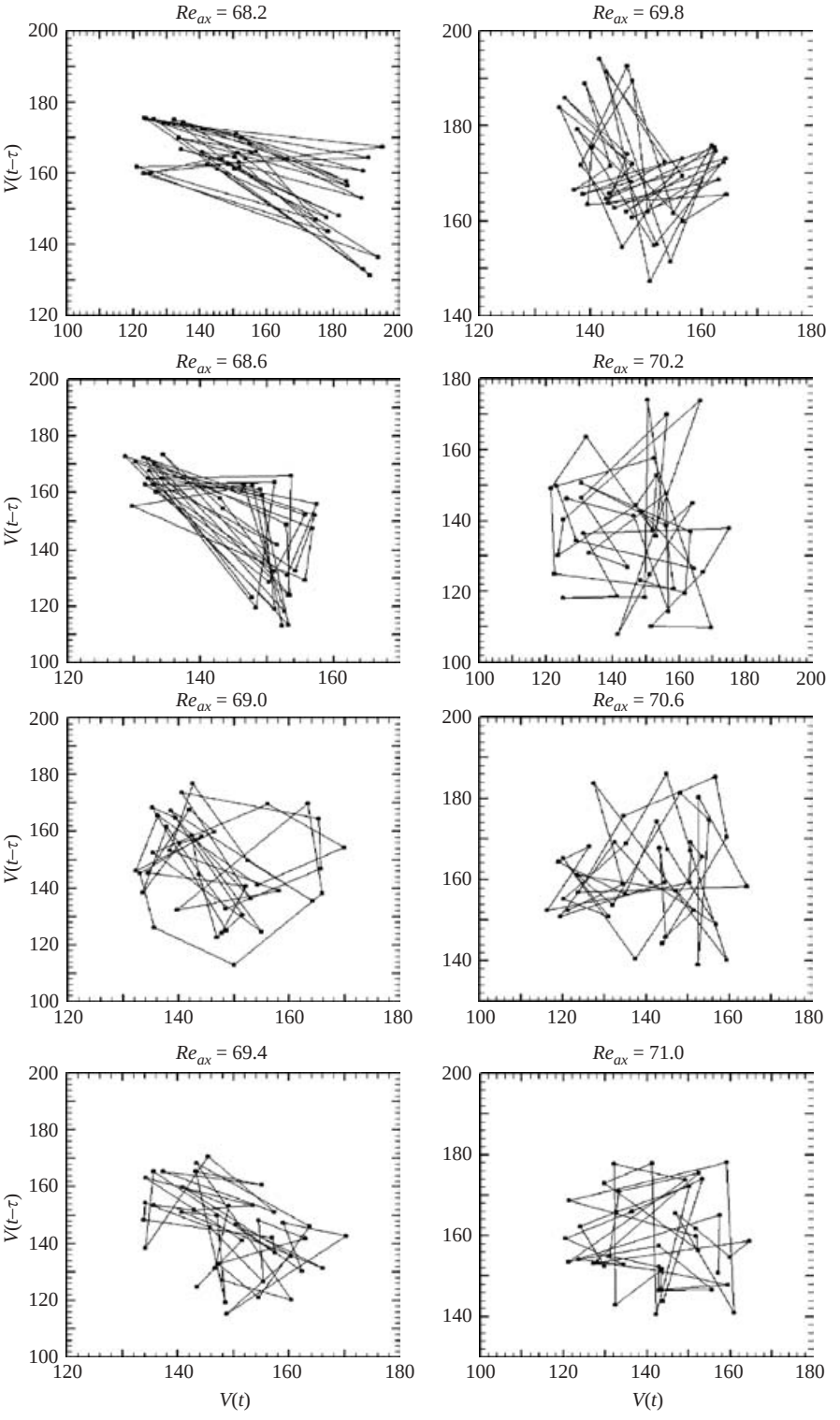

FIGURE 19. Poincaré maps for $Re_{ax} = 68.2$ to 71.0, at constant $Re_{\Omega} = 244.0$.

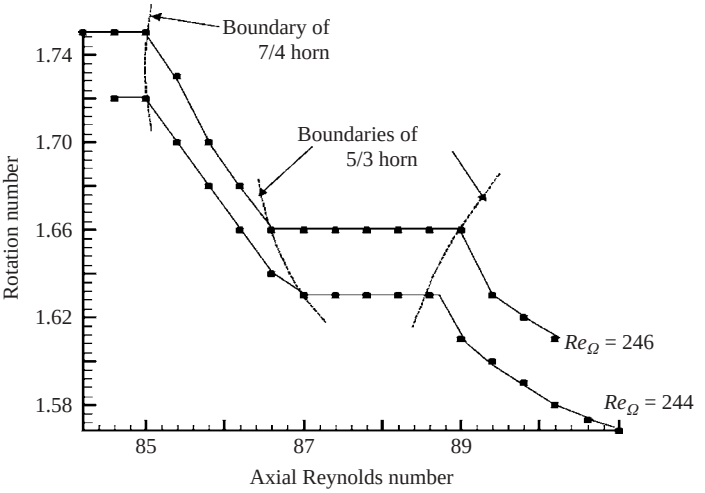

FIGURE 20. Rotation number plot for two parametric cuts at $Re_\Omega = 244$ and 246. The data for $Re_\Omega = 244$ have been shifted for clarity.

The clusters remain topologically similar until the end of the cut at $Re_{ax} = 71.0$, and the rotation number as computed from the power spectrum reduces apparently monotonically from one location to the next. The smaller resonances contained in this region are not clearly identified at our experimental resolution.

The parametric cut at $Re_\Omega = 244$ has thus identified regions of frequency-locking and apparent quasi-periodicity, and located their respective boundaries. This global behaviour agrees well with the known existence of alternating bands of frequency-locking and quasi-periodicity in the postcritical regime of a Neimark–Sacker bifurcation. The cut at $Re_\Omega = 246$ confirmed the gradual nonlinear growth of the horn boundaries.

The experiments did not identify any hysteresis effects at the edge of the horns, but the step in Re_{ax} may have been too large, and the noise level too high. In other experimental studies, such as Ecke & Kevrekidis (1988), secondary Hopf bifurcations were identified within individual resonance horns, and attractors were found to undergo wrinkling and other topological changes. The parametric cuts described here did not capture any such phenomena.

4.6. *Rotation number plot*

The data presented in the previous section can be summarized in a rotation number plot (figure 20). The horizontal (fixed rational rotation number) sections indicate frequency-locking while the inclined (apparently continuously changing 'irrational' rotation number) sections suggest quasi-periodicity. Higher-order resonances in this regime are not discernible within the experimental resolution. The growth of the resonance horns with increasing rotational Reynolds number is indicated by the dashed lines. The 5/3-horn has been fully captured while only part of the 7/4-horn has been captured. Owing to the nonlinear shape of the horns in parameter space, it is not possible to extrapolate how they appear with increasing distance from the critical surface. Figure 21 shows how the Poincaré section changes character for a few specially selected points on the rotation number plot.

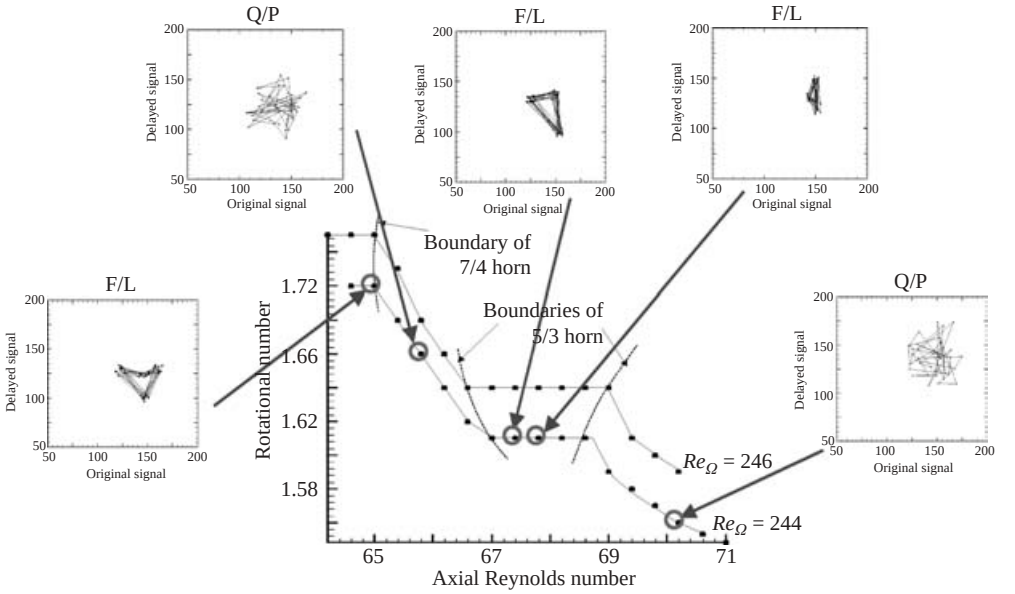

FIGURE 21. Global variation of the qualitative nature of the Poincaré section at different points in parameter space. For clarity, only a few selected points are shown, F/L, frequency locking; Q/P, quasi-periodic.

5. Postcritical axial and azimuthal wavenumber: preliminary results

In order to map the spatial development of the system postcritical behaviour, large regions above the critical curve were investigated, identified by the entire region above the critical curve in figure 11, from Re_{ax} of 0 to 100, encompassing transitions to quasi-periodic flows (shaded region) and periodic flows (unshaded region). Note that the study of the bifurcation dynamical properties was restricted to the shaded region only. Referring to figure 11, we proposed to study the response of wavy vortex flow to increasing axial forcing (path AB), the response of some non-axisymmetric $n \neq 0$ mode located just above the critical surface to increasing rotation rates (path CD), and the possible correlation among changes in the postcritical spatial structure and temporal dynamics.

5.1. *Variation of axial wavenumber*

The experimentally determined axial wavenumber for the (unforced) transition from circular Couette flow to Taylor vortex flow is 3.118, in excellent agreement with the value of 3.129 obtained from Floquet analysis by Marques & Lopez (1997).

For forcing amplitudes up to $Re_{ax} \approx 40$, the axial wavenumber changes very little; small decreases are balanced almost equally by small increases. However, for $Re_{ax} > 40$ the trend is markedly different. The axial wavenumber rises rapidly by about 45 % from $Re_{ax} = 40$ to 80. As mentioned by Wereley & Lueptow (1998), an increased amplitude of forcing could result in an increased amount of fluid transport between individual cells, thereby generating direct competition between Couette flow and Stokes flow. The primary bifurcation in circular Couette flow leads to a flow with axial wavenumber π while the primary bifurcation in annular Stokes flow has an infinite wavelength (wavenumber zero), that is, it does not undergo an instability with finite length scale. Thus, as the axial component increases, it is plausible that the

connection between the two modes leans more heavily in favour of Stokes flow and to a reduced axial wavenumber. This occurs to some degree for Re_{ax} up to about 40. Why a further increase in the Stokes component appears to initiate a dramatic rise in axial wavenumber is not clear. Perhaps the two components begin to interact in a complicated manner with the increasing axial momentum transport, or perhaps we experience another bifurcation. Further experiments are necessary to resolve this question.

For Re_{ax} up to about 30, there is a generally slow decrease in axial wavenumber for Re_{Ω} less than about 200. Between Re_{Ω} of 200 and 250, the axial wavenumber varies unpredictably without any clear pattern, while above Re_{Ω} of 250 it generally rises monotonically. For Re_{ax} equal to 50 and 60, an initial rapid increase is observed, followed by a gradual reduction to about the initial value of k. However, for Re_{ax} of 70 and 80 we observe only a steep rise in k.

5.2. *Variation of azimuthal wavenumber*

The $n = 1$ azimuthal mode is not observed in the presence of finite-amplitude forcing. Any given azimuthal mode is observed for a small interval in azimuthal Reynolds number only; modes appear and disappear with a change in $Re_{\Omega} = 10$, which also means that the boundaries between distinct azimuthal modes are known only to values of Re_{Ω} within ± 10. Furthermore, the effect of a sudden jump in azimuthal Reynolds number on the existing flow state is unclear. Observations indicate that once a given wavy mode is established, increasing axial forcing does not reduce the azimuthal wavenumber. Rather, the amplitude of the waviness in the vortex structures is reduced until it is virtually undetectable close to the transition surface, typically within an Re_{ax} of 10 above criticality. According to Marques & Lopez (2000), axial oscillations of the inner cylinder destabilize the non-axisymmetric wavy modes. Our observations suggest that such forcing leads to the gradual emergence of inhomogeneities within the flow pattern, which may be interpreted as a physical manifestation of the destabilization of the vortex pattern. Occasional vortex 'mis-matches', appearing qualitatively similar to vortex dislocations, become more common as the forcing amplitude is raised.

5.3. *Three-dimensional reconstruction of axial wavenumber development*

Figure 22 shows the variation of axial wavenumber beyond the primary critical curve (the contour lines are for fixed axial wavenumber k). Narrow strong variations in axial wavenumber are observed, with some regions displaying a more pronounced localized change in k than others. The zone containing the steepest gradients generally occurs in the upper-right corner of the region of investigation. Comparison with figure 11 reveals that the steepest gradients are thus found near the (expected) boundaries of the $n = 1$ region.

Up to about $Re_{ax} = 40$, changes in axial wavenumber are relatively insignificant compared with other regions. For all Re_{ax} in excess of about 50, a rapid rise in axial wavenumber is evident. However, superimposed on this overall rapid rise are localized regions where even steeper gradients exist ($50 < Re_{ax} < 80$). Figure 22(b) shows a close-up of this region.

The figure suggests that the region containing transition to quasi-periodic flow (the shaded area in figure 11) closely coincides with the region exhibiting steep gradients in axial wavenumber in figure 22. Indeed, the steepest gradients in k appear to lie near the boundaries of the Neimark–Sacker bifurcation. This is in accordance with Marques & Lopez (2000) who state that a feature of this type of bifurcation is the simultaneous emergence of multiple spatial mode – the nonlinear interaction of which leads to

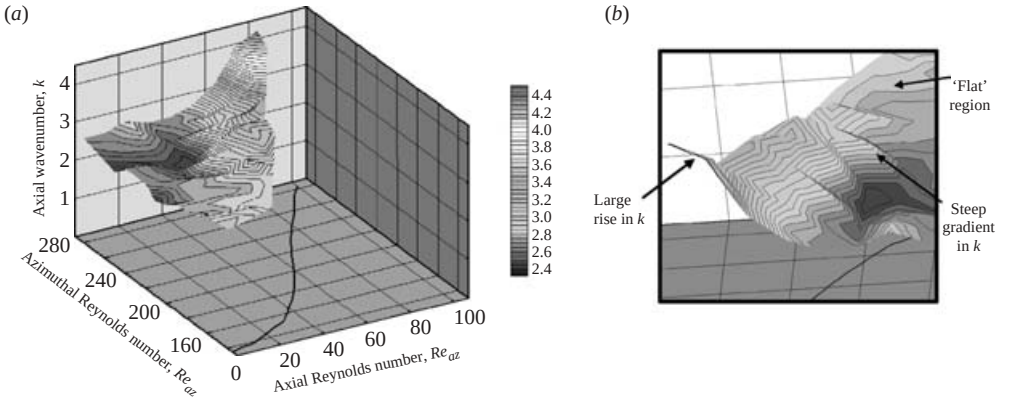

FIGURE 22. Effect of increasing rotation rate on azimuthal wavenumber beyond the primary transition. The curve drawn in the (Re_{ax}, Re_{az})-plane is the stability boundary shown in figure 11. The location of the large gradients observed in (*a*) and the shaded region in figure 11 correlate very well with each other. The close-up in (*b*) is obtained when viewed from the far side of the critical surface.

practically discontinuous or essentially very steep changes in axial wavenumber as well as discrete jumps in azimuthal wavenumber. The three-dimensional plot reveals a large rapid rise in k, which nearly coincides with the Neimark–Sacker bifurcation boundary. It is not possible to determine with certainty whether the rapid rise in axial wavenumber is actually discontinuous (it would not be in an experiment). It appears to be continuous in the present experiment, but it should be noted that the jump size from one point to the next is the same as the interval over which the very large gradients are observed. A higher-resolution survey is required in order to locate the span of the jump.

5.4. *Spatial changes to the flow structure*

Figure 23 illustrates the response of the flow structure to increasing axial forcing. Figure 23(*a*) is for zero forcing ($Re_{ax} = 0$) while figures 23(*b*) to 23(*d*) are for increasing forcing amplitude. The interaction between the axisymmetric forcing and the wavy vortex flow generates a non-axisymmetric flow state. At $Re_{ax} = 0$, we note the regular appearance of azimuthal waves of high amplitude on the closed vortex rings. A small but finite amount of forcing, however, leads to a sharp change, localized in space, in the qualitative structure of the flow; the wavy closed rings break to form open wavy spirals, leading to a new azimuthal symmetry. This breaking leads to azimuthal wavenumbers (which represent the number of azimuthal waves per vortex spiral) that are no longer restricted to integral values from rotational symmetry arguments. The relaxing effect that this extra degree of freedom brings to the flow is unclear. By $Re_{ax} = 40$, the amplitude of cell waviness has reduced and local inhomogeneities are observed. At $Re_{ax} = 60$, we observe an increased vortex spiral inclination and (possibly fortuitous) reduction in spatial inhomogeneities. The bottom image (maximum axial forcing) contains a higher axial wavenumber than the top image (zero axial forcing) which is consistent with figure 22(*a*). Even for small forcing amplitudes, say $Re_{ax} = 20$, the vortex structures appear to be slightly inclined. As the forcing amplitude rises, the amplitude of the cell waviness reduces while the azimuthal wavenumber appears to be unchanged.

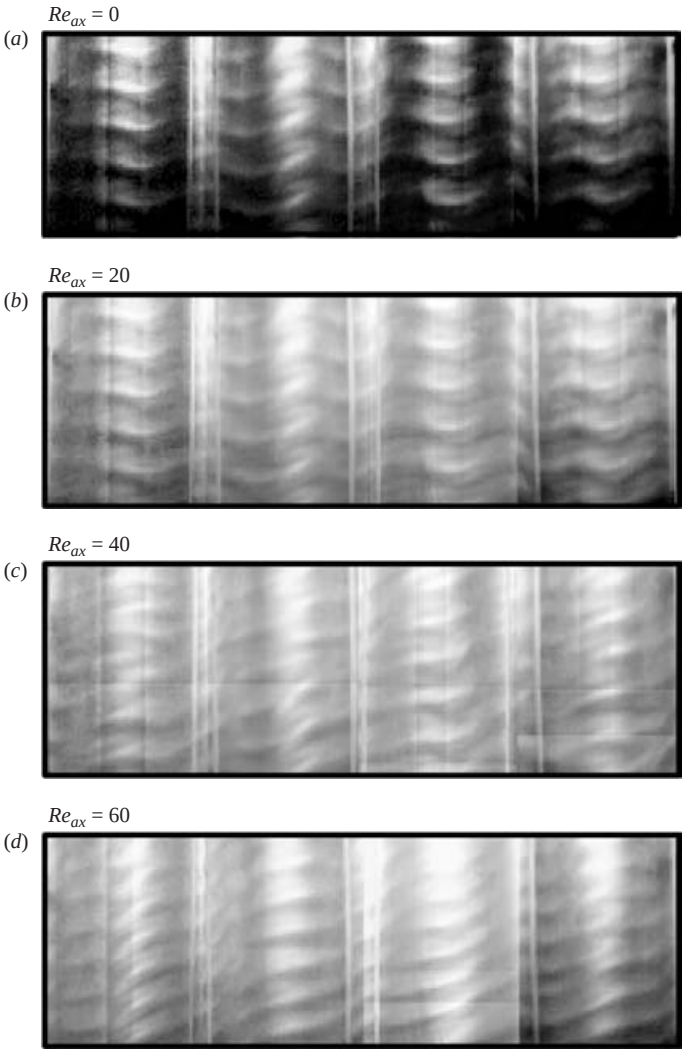

FIGURE 23. Surround images showing the effect of increasing axial forcing on wavy vortex flow. The increasing forcing amplitude breaks the closed rings into open wavy spirals.

6. Conclusions

A Hopf (Neimark–Sacker) bifurcation to a T^2 torus has been observed in axially forced Taylor–Couette flow. The flow instability results in time-varying open Taylor spirals at an inclination to the cylinder axis, and this inclination varies sinusoidally with time. Two bifurcating modes with azimuthal wavenumbers I and II were identified. The vortex topology of the stable bifurcated flow exhibits strong axial and azimuthal periodicity. Above the primary transition surface, the axial forcing rapidly destabilizes the Taylor cells into a spatiotemporally chaotic flow. For both modes there were no hysteresis effects, implying a supercritical transition.

The temporal dynamics of the flow were characterized through power spectra and delay-reconstructed Poincaré maps. Depending upon the exact location in three-dimensional parameter space, the flow exhibited alternating bands of frequency-locking and quasi-periodicity. The growth of major resonance horns in parameter

space away from the critical surface was also mapped out. The horns studied were not observed to interact in this study, since the dynamics of the flow were not explored sufficiently far beyond the instability threshold. In the postcritical regime beyond the primary transition surface, the axial wavenumber variation was relatively small over most of the parameter space. In a localized region, however, very large gradients in axial wavenumber were found that were well correlated to the expected boundaries of the Neimark–Sacker bifurcation for this flow. The experiments also captured the physical manifestations of the bifurcated flow states and their subsequent destabilization. The flow structure remained axially and azimuthally periodic close to the bifurcation curve. The axial forcing gradually destabilized the wavy Taylor spirals observed at criticality and permitted regions of chaotic flow, characterized by markedly reduced periodicity, to form at random points in the flow.

Stimulating discussion with F. Marques and J. M. Lopez are appreciated. The use of sliced stacks was suggested by J. J. Allen. The work was supported by the NSF through Grant CTS97-06902 and the AFOSR (Dynamics and Control, Dr B. King).

REFERENCES

Andereck, C. D., Liu, S. S. & Swinney, H. L. 1986 Flow regimes in a circular Couette system with independently rotating cylinders *J. Fluid Mech.* **164**, 155–183.

Bendat, J. S. & Piersol, A. G. 1966 *Measurement and Analysis of Random Data.* Wiley.

Benjamin, T. B. & Mullin, T. 1981 Anomalous modes in the Taylor experiment. *Proc. R. Soc. Lond.* A **377**, 221–249.

Bergé, P., Pomeau, Y. & Vidal, C. 1984 *Order within chaos: Towards a Deterministic Approach to Turbulence.* John Wiley.

Chiffaudel, A. & Fauve, S. 1987 Strong resonance in forced oscillatory convection. *Phys. Rev.* A **35**, 4004–4007.

Cole, J. A. 1976 Taylor-vortex instability and annulus-length effects. *J. Fluid Mech.* **75**, 1–15.

Coles, D. 1965 Transition in circular Couette flow. *J. Fluid Mech.* **21**, 385–425.

Davis, S. H. 1976 The stability of time-periodic flows. *Annu. Rev. Fluid Mech.* **8**, 57–74.

Dominguez-Lerma, M. A., Ahlers, G. & Cannell, D. S. 1985 Effects of Kalliroscope flow visualization particles on rotating Taylor–Couette flow. *Phys. Fluids* **24**, 1204–1206.

Donnelly, R. J. 1960 Experiments on the stability of viscous flow between rotating cylinders III. Enhancement of stability by modulation. *Proc. R. Soc. Lond.* A **181**, 130–139.

Ecke, R. E. & Kevrekidis, I. G. 1988 Interactions of resonances and global bifurcations in Rayleigh–Bénard convection. *Phys. Lett.* A **131**, 344–352.

Glazier, J. A. & Libchaber, A. 1988 Quasi-periodicity and dynamical systems: an experimentalist's view. *IEEE Trans. Circuits Syst.* **35**, 790–809.

Guckenheimer, J. & Holmes, P. 1983 *Nonlinear Oscillations, Dynamical Systems, and Bifurcation of Vector Fields.* Springer.

Hu, H. C. & Kelly, R. E. 1995 Effect of time-periodic axial shear flow upon the onset of Taylor vortices. *Phys. Rev.* E **51**, 3242–3251.

Kai, T., & Tomita, K. 1979 Stroboscopic phase portrait of a forced nonlinear oscillator. *Prog. Theor. Phys.* **61**, 54–73.

Kevrekidis, I. G., Schmidt, L. G. & Aris, R. 1986 Some common features of periodically forced reacting systems. *Chem. Engng Sci.* **41**, 1263–1276.

Marques, F. & Lopez, J. M. 1997 Taylor–Couette flow with axial oscillations of the inner cylinder: Floquet analysis of the basic flow. *J. Fluid Mech.* **348**, 153–175.

Marques, F. & Lopez, J. M. 2000 Spatial and temporal resonances in a periodically forced hydrodynamic system. *Physica* D **136**, 340–352.

Marques, F., Lopez, J. M., & Iranzo, V. 2002 Imperfect gluing bifurcation in a temporal glide-reflection symmetric Taylor–Couette flow. *Phys. Fluids* **14**, L33–L36.

Ning, L. 1991 Instabilities and patterns in Taylor–Couette flow. PhD thesis, University of California, Santa Barbara.

Packard N. H., Crutchfield, J. P., Farmer, J. D. & Shaw, R. S. 1980 Geometry from a time series. *Phys. Rev. Lett*. **45**, 712.

Pavlou, S. & Kevrekidis, I. G. 1992 Microbial predation in a periodically operated chemostat: a global study of the interaction between natural and externally imposed frequencies. *Math. Biosci*. **108**, 1–55.

Savas, O. 1985 On flow visualization using reflective flakes. *J. Fluid Mech*. **152**, 235–248.

Sinha, M. 2003 Spatio-temporal dynamics of periodically forced rotating flows. PhD thesis, Princeton University.

Stevens, J. L., Lopez, J. M. & Cantwell, B. J. 1999 Oscillatory flow states in an enclosed cylinder with a rotating endwall. *J. Fluid Mech*. **389**, 101–118.

Swift, J. W. & Wiesenfeld, K. 1984 Suppresion of period-doubling in symmetric systems *Phys. Rev. Lett*. **52**, 705.

Takens, F. 1981 *Strange Attracttors in Turbulence: Dynamical Systems and Turbulence*, Springer. pp. 366–381.

Weisberg, A. Y. 1996 Control of transition in Taylor–Couette flow with axial motion of the inner cylinder. PhD thesis, Princeton University.

Weisberg, A. Y., Kevrekidis, I. G. & Smits, A. J. 1997 Delaying transition in Taylor–Couette flow with axial motion of the inner cylinder. *J. Fluid Mech*. **348**, 141–151.

Wereley, S. T. & Lueptow, R. M. 1998 Spatio-temporal character of non-wavy and wavy Taylor–Couette flow. *J. Fluid Mech*. **364**, 59–80.